RESEARCH ARTICLE
PLANETARY SCIENCES

Earth and Planetary Physics
6: 495–521, 2022
doi: 10.26464/epp2022049

Impacts of thrusting, extensional faulting, and glaciation on cratering records of Pluto's largest moon Charon: Implications for the evolution of Kuiper belt objects

HanZhang Chen*, and An Yin*

Department of Earth, Planetary, and Space Sciences, University of California, Los Angeles, California 90095-1567, USA

Key Points:

- Geomorphologic mapping of Charon's encountered hemisphere reviews a landform assemblage likely generated by regional glaciation.
- Craters truncated by arcuate scarps may have resulted from thrusting.
- Interpreted glaciation and thrusting have strongly modified the occurrence and shape of craters on Charon.

Citation: Chen, H. Z., and Yin, A. (2022). Impacts of thrusting, extensional faulting, and glaciation on cratering records of Pluto's largest moon Charon: Implications for the evolution of Kuiper belt objects. *Earth Planet. Phys.*, *6*(6), 495–521. http://doi.org/10.26464/epp2022049

Abstract: A first-order question in the studies of the Solar System is how its outer zone known as the Kuiper belt was created and evolved. Two end-member models, involving coagulation vs. streaming instability, make different predictions—testable by the cratering history of Kuiper Belt Objects (KBOs)—about the cumulative size-frequency distribution (SFD) of the KBOs. Among all of the imaged KBOs, Pluto's largest icy moon, Charon, appears to preserve the largest size range of seemingly undisturbed craters, their diameters (D) on Charon ranging from < 1 km to > 220 km. Current work shows that Charon's craters with D < 10–20 km are fewer than those expected by the coagulation mechanism, but whether this is an artifact of post-cratering modification of smaller craters is unknown. We address this issue by conducting systematic photogeological mapping and performing detailed landform analysis using the highest resolution images obtained by the New Horizons spacecraft, which reveal a range of differentiable terrains on Charon. The most important findings of our work include (1) truncation and obliteration of large craters (diameters > 30–40 km) and their crater rim ridges along the eastern edges of several north-trending, eastward-convex, arcuate ranges in Oz Terra of the northern encountered hemisphere, (2) lobate ridges, lobate knob trains, and lobate aprons resembling glacial moraine landforms on Earth, (3) dendritic channel systems containing hanging valleys, and (4) locally striated surfaces defined by parallel ridges, knob trains, and grooves that are > 40–50 km in length. The above observations and the topographic dichotomy of Charon's encountered hemisphere can be explained by a landscape-evolution model that involves (i) a giant impact that created the Vulcan Planitia basin and the extensional fault zone along its northern rim, (ii) a transient atmosphere capable of driving N_2-ice glacial erosion of the water-ice bedrock and transporting water-ice debris to sedimentary basins, (iii) regional glacial erosion and transport of earlier emplaced impact ejecta deposits from the highlands of Oz Terra into the lowland basin of Vulcan Planitia, (iv) syn-glaciation north-trending thrusting, interpreted to have been induced by Charon's despinning, and (v) the development of a water-ice debris cover layer over subsurface N_2 ice below Vulcan Planitia during global deglaciation. The infilling of the Vulcan Planitia could have been accompanied by cryovolcanism. The extensive modification of impact craters means that the size-frequency distributions of Charon's craters should serve only as a lower bound when used to test formation mechanisms proposed for Kuiper belt objects.

Keywords: Kuiper belt; geomorpgology; Charon; glacier; thrusting

1. Introduction

Understanding the formation of the Kuiper belt is central to quantifying the dynamic evolution of the Solar System (Nesvorný, 2018). A starting point of this endeavor is to establish the cumulative size-frequency distribution (SFD) and evolution of Kuiper Belt Objects (KBOs), which can be used to test competing models of planet formation during the initial < 100-Myr development of the Solar System (Youdin and Goodman, 2005; Schlichting et al., 2013; Abod et al., 2019; Morbidelli et al., 2021). To this end, current understanding of the KBO size distribution comes from two independent sources of observations: (i) telescopic surveys (Schlichting et al., 2012; Fraser et al., 2014), and (ii) crater records of recently imaged KBOs by the New Horizons spacecraft (Robbins et al., 2017; Singer et al., 2019; Spencer et al., 2020). Among the imaged KBOs, Charon, Pluto's largest icy moon, appears to preserve the largest size range of seemingly undisturbed craters, their diameters

Correspondence to: H. Z. Chen, hanzchen@g.ucla.edu
A. Yin, ayin54@gmail.com
Received 25 AUG 2022; Accepted 13 OCT 2022.
Accepted article online 11 NOV 2022.

(D) on Charon ranging from < 1 km to > 220 km. Detailed crater mapping and size counting show a significant deficit of D < 10–20 km when compared to the projected trend of the KBO sizes determined by the telescopic surveys (Singer et al., 2019). This deficit is expressed by a gentler slope for craters with D = 2–13 km than the slope for craters with D = 13–30 km in the plot of cumulative crater numbers vs. crater diameters (Robbins et al., 2017; Singer et al., 2019). The deficit of smaller craters implies collisional disequilibrium of the KBOs that have sizes smaller than 1–2 km across. This inference is contrary to the coagulation models, which predict KBOs to have entered a state of collisional cascade within the first ~100 million years (Myr) of Solar System history (Stern, 1995; Farinella and Davis, 1996; Schlichting and Sari, 2011; Schlichting et al., 2013). The discrepancy, however, could be explained by neglect of ice strength in early coagulation models (Kenyon and Bromley, 2020), or streaming instabilities during the formation of KBOs (Youdin and Goodman, 2005; Abod et al., 2019). The last explanation has been favored by Singer et al. (2019).

The coagulation vs. streaming-instability KBO formation hypotheses can be tested by the cratering record on Charon. For example, the crater SFD reported by Robbins et al. (2017) and Singer et al. (2019) could have been affected by later resurfacing events (Morbidelli et al., 2021). If so, a coagulation mechanism cannot be rejected. On the other hand, a streaming-instability mechanism would be supported if the reported crater SFD has not been disrupted by younger geological events (Singer et al., 2019).

In this study, we address systematically the critical issue of whether the crater record of Charon has been modified by later geological processes. To do so, we have performed detailed geomorphological mapping across the entire encounter hemisphere of the satellite, at the highest resolution to date. Our mapping is accompanied by detailed landform analyses; the formation mechanisms suggested by the analyses are supported by well-documented, well-understood analogues from Earth, Mercury, and Mars. We conclude that most craters on Charon have been modified by previously unrecognized geological processes such as thrusting, extensional faulting, glaciation, crater-filling viscous flows, and possible fluvial processes. This detailed new understanding in turn implies that crater size-frequency data from Charon should be regarded only as a lower bound when used to test competing models of Kuiper-belt formation.

2. Pluto–Charon System

The Pluto–Charon system has been interpreted to have been formed by the collision of two similarly sized progenitors within the first 10 Myr of the Solar System history (McKinnon, 1989; Canup, 2005; Canup et al., 2021; McKinnon et al., 2021). The distribution of their spin/orbital periods and the small eccentricity of the Pluto–Charon system favor an explanation that Pluto and Charon were fluid-like at the onset of their formation, which implies that the two bodies had experienced rapid differentiation at the time of their initial formation (Arakawa et al., 2019). Thermal-modeling results show that such early differentiation should lead to the formation of ancient subsurface oceans within the two bodies, and that Charon's should have been refrozen by ca. 4.0 billion years (Ga) (Desch and Neveu, 2017) or 2.5–2.0 billion years ago (Ga) (Desch and Neveu, 2017; Bierson et al., 2018), depending on the nature and evolution of the assumed heat sources. Because Pluto has a N_2-dominated atmosphere, the assumption of a shared origin with its largest moon implies that Charon may also have had a primordial N_2 atmosphere. This inference was anticipated from theoretical considerations (Trafton et al., 1988) and the current understanding of Kuiper belt history (e.g., Stern et al., 2015). Such a scenario is likely, because Charon's initial surface temperature is considered to be at ~100 K, possibly induced by the combination of a closer distance to the Sun (Nesvorný, 2018) and the release of heat from the Charon-forming collision (Canup et al., 2021; McKinnon et al., 2021), gravitational accretion (Canup et al., 2021; McKinnon et al., 2021), radiogenic decay (Canup et al., 2021; McKinnon et al., 2021), internal phase changes (Malamud et al., 2017; Canup et al., 2021; McKinnon et al., 2021), and tidally induced deformation (Stern and Trafton, 2008; Rhoden et al., 2020; Conrad et al., 2021). If the atmospheric and surface vapor pressures were in equilibrium, a surface temperature (T) higher than nitrogen melt temperature of 63.15 K would imply surface vapor pressures of >100 μbar for the dominant KBO volatile species such as N_2, CO, and CH_4 (Fray et al., 2009). The above pressure and temperature conditions on Charon could have resulted in fluvial processes involving N_2 liquid. As a result of atmosphere escape, the subsequent surface temperature on Charon after its initial formation should have decreased below the freezing temperature of N_2 liquid, which would have favored N_2-ice glaciation on the surface of Charon. Glaciation on Charon is possible when considering the occurrence of past and current glaciation on Pluto (Howard et al., 2017) and the fact that the current N_2 vapor pressures on Pluto are 10^{-2} to 10^3 μbar, inferred from theoretical modeling (Hansen and Paige, 1996) and actual measurements (Gladstone et al., 2016; Bertrand et al., 2018; Johnson et al., 2021), which are comparable to the pressure magnitudes deduced from theoretical considerations (Trafton et al., 1988).

However, previous studies have interpreted Charon's landscape as having evolved mainly through cratering, global extension, and cryovolcanism (Moore et al., 2016; Desch and Neveu, 2017; Beyer et al., 2019; Robbins et al., 2019; Spencer et al., 2021), contrary to the expected primordial atmosphere over early Charon as inferred by Trafton et al. (1988). Although the above inferred geologic processes explain a large number of observations from Charon, they are unable to account for the following observations:

(1) Larger craters (D > 50 km) consistently lack ejecta blankets and secondary craters (Moore et al., 2016; Robbins et al., 2017, 2019; Protopapa et al., 2021). This observation requires a geological process capable of removing the impact-generated materials and landforms, which has not been discussed in the current literature.
(2) Trough networks dominate Oz Terra on Charon (Moore et al., 2016; Beyer et al., 2017); the assigned normal-faulting mechanism (Beyer et al., 2017) does not explain converging dendritic-like trough networks and locally highly curvilinear trough traces (see more details below).
(3) The origin of the topographic dichotomy boundary between Oz Terra and Vulcan Planitia (Figures 1a and 1b) in the encounter hemisphere of Charon has been attributed to a giant impact (Malamud et al., 2017) or zonal extension (Beyer et al., 2019).

Current observations challenge both hypotheses: the impact hypothesis does not explain the lack of impact breccias; the extension hypothesis does not explain why faulting is localized along the rim of Vulcan Planitia.

(4) No explanation has been offered for the exposure of higher volume contents and larger grain sizes of crystalline water ice that are uniquely restricted along north-trending ranges in Oz Terra (Protopapa et al., 2021). As noted below, the exposures of crystalline water ice are exclusively associated with arcuate ranges that truncate $D > 50$ km craters.

The above unresolved issues suggest that additional geological processes have contributed to the geomorphological development of Charon. For example, the lack of impact breccias around the largest craters on Charon requires erosion and transport processes; the inconsistency in explaining the dichotomy boundary implies that the shaping of Charon's morphologies may require even more complicated geologic processes.

3. Data and Methods

Images collected by the Long-Range Reconnaissance Imager (LORRI; Cheng AF et al., 2008) and Multi-spectral Visible Imaging Camera (MVIC) (Reuter et al., 2008; Howett et al., 2017) on board of the New Horizons spacecraft are used in our geomorphological mapping (Schenk et al., 2018a). Landform analyses are assisted by the use of digital elevation models (DEMs) created by Schenk et al. (2018a). The resolutions of the images used in this study vary from ~154 m/pixel to ~1460 m/pixel. Meanwhile, the DEMs used in this study have a uniform map-view resolution of 300 m/pixel (Schenk et al., 2018a; Robbins et al., 2019).

The shape and distribution of each mapped landform was determined by using both the satellite image and corresponding DEM at each location. By doing so, we have been able to minimize artifacts created by the spatial variation in pixel scales, solar incident angles, viewing directions of three-dimensional objects, and emission angles (Schenk et al., 2018a). All DEMs used in this study are geographically rectified and shown in a cylindrical projection. According to Schenk et al. (2018a), the horizontal resolution of the DEMs is ~300 m/pixel. In contrast, the vertical resolution is ca. 100–400 m for most of the area covered in this study except rim regions where resolutions degraded to ~1500 m (see Fig. 4 in Schenk et al., 2018a). Note that all topographic profiles presented in this report have vertical uncertainties of < 500 m (Figures 2 and 9).

Geological mapping was conducted on the highest resolution images available; the resulting maps were drafted using Adobe Illustrator™. Analogue examples from Earth were taken from images available from published work and Google Earth™, whereas analogue examples from Mars and Mercury are taken from NASA's publically accessible data.

Images used for mapping were first processed using Adobe Photoshop™ for the best display of their brightness and contrast. Because of this, caution should be taken by readers when comparing the images used in this study with their unprocessed counterparts taken directly from NASA's database. Because craters on Charon were mapped in detail by Robbins et al. (2017), Singer et al. (2019), and Robbins and Singer (2021), our mapping does not repeat this effort but focuses instead only on selected craters that illustrate different cratering styles and different relationships between the mapped craters and surficial landforms and/or surficial materials next to the craters.

Interpreting the formation mechanism of a single element in a geological system often yields highly non-unique solutions; such a narrowly focused investigation rarely answers central scientific questions. Because of this, we do not offer interpretations of each terrain after its description, as commonly done by researchers in the planetary geology community. Rather, we have adopted the land system approach (e.g., Brodzikowski and Van Loon, 1987; Yin A et al., 2021), aiming at constructing the first-order landscape-evolution model of Charon, presented below, that can account for the spatiotemporal relationships among all facets and all elements in the analyzed geomorphological system, as constrained by our systematic and detailed mapping.

4. Results of Geomorphologic Mapping

Based on a systematic landform analysis, we have used available data to constrain the spatiotemporal relationships among all geomorphological features in Charon's encounter hemisphere. Figure 1A is an enhanced color view of Charon that combines blue, red, and infrared images taken by the New Horizons spacecraft's Ralph/Multispectral Visual Imaging Camera (MVIC) (Moore et al., 2016). Figure 1B is a digital elevation model of Charon's encounter hemisphere, at a horizontal resolution of 300 m/pixel, overlying the Charon New Horizons LORRI MVIC Global Mosaic 300 m v1 (Schenk et al., 2018a). Figure 1C is a geomorphological map of Charon's encounter hemisphere created in this study. Description of landform units is listed in the column to the right of the figure.

Our geomorphological mapping is built upon the early studies of Charon (Moore et al., 2016; Desch and Neveu, 2017, Beyer et al., 2019; Robbins et al., 2019; Beddingfield et al., 2019), but differs from them in the following two ways. First, we separate elongated linear and curvilinear depressions (i.e., troughs) into two types: those bounded by flat plains (e.g., Feature 6 in Figure 1B) and those bounded by rift-shoulder-like ridges (e.g., Feature 3 in Figure 1B) (cf., Desch and Neveu, 2017; Beyer et al., 2019). Second, we split the *two* landform units previously mapped in Oz Terra by Beyer et al. (Desch and Neveu, 2017; Beyer et al., 2019) and Robbins et al. (2019) into *ten* differentiable terrains (Figure 1C). This more-detailed terrain classification allows us to suggest landform-formation mechanisms that are more comprehensive and self-consistent. Description of the mapped units, their correlations with earlier mapped terrains, and their temporal relationships (i.e., chronostratigraphy) are summarized in Figures. 1C and 1D.

4.1 Landform Units

We describe the landforms units in our regional geomorphological map (Figure 1C) based on their formation ages from the oldest to the youngest.

Unit ct_1. This unit has Charon's the oldest and largest-sized craters, characterized by degraded crater-basin morphologies, such as lack of central uplifts and rim ridges, and also marked by a total

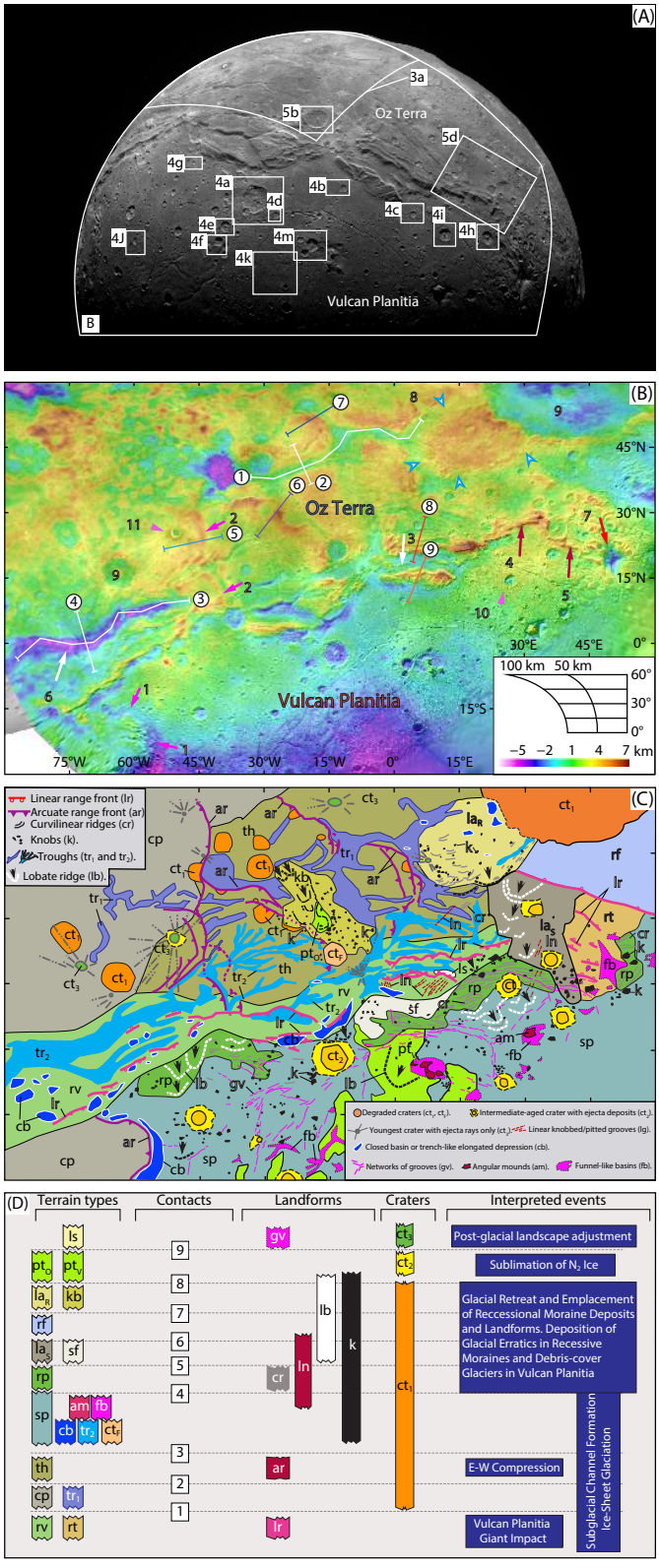

ls Lobate-apron shaped landforms occurring at the base of linear ridge scarps and interpreted as landslides by Beddingfield et al. (2019).

gv Networks of rill-like grooves cutting across Vulcan Planitia, displaying en echelon alignment, and intersecting into Y-shaped triple junctions; this groove feature is the same as that described in Moore et al. (2016), Beyer et al. (2019) and Robbins et al. (2019).

pt_o pt_v Pitted terrain with circular or oval depressions in Oz Terra (O) and Vulcan Planitia (V). This unit correlates approximately to the mottled terrain "Mt" of Robbins et al. (2019).

k Knobs of various sizes (1–10 km) and shapes (rectangular, polygonal, circular, and oval) concentrated mostly in Vulcan Planitia but also in Oz Terra; it correlates locally with the mons unit "Moa" of Robbins et al. (2019).

lb Lobate ridges locally dotted by angular and circular knobs along ridge crests; they are dominantly convex southward.

la_R Rough-surfaced lobate-apron plateau that locally display parallel ridges and furrows.

kb Knobbed terrain characterized by the presence of angular to circular knobs and parallel curvilinear ridges.

rf A rough-floored basin bounded by a linear scarp in the south and Dorothy crater in the northwest.

ln Parallel linear grooves and ridges exposed on larger planar ridge flanks that bound the northern edge of Vulcan Planitia; the grooves are interrupted by small knobs within the linear depressions or defined by linked pits; this unit was mapped as grooves by Beyer et al. (2019) and scarp crests by Robbins et al. (2019).

la_s Smooth-surfaced lobate-apron landforms in the southeastern corner of Oz Terra.

sf Smooth terrain in Vulcan Planitia characterized by superposed ridges, grooves, and knobs on the smooth surface.

cr Parallel linear and curvilinear ridges and furrows mingled with similarly shaped lobate ridges (lb) along the northern margin of Vulcan Planitia; the furrows are marked as grooves by Moore et al. (2016), Beyer et al. (2019), and Robbins et al. (2019).

rp Ridged plains terrain best developed along the northern margin of Vulcan Planitia and intermingled with southward-convex lobate ridges that expose angular blocks along the ridge crests.

fb Funnel-like and commonly polygonal shaped depressions characterized by downward-steepening, cylindrical-shaped rims and antiformal-synformal ridges and troughs emanating from the corners of the depressions; the antiformal ridges are referred to as the "broad warps" by Beyer et al. (2019), and Robbins et al. (2019); the unit correlates roughly with "depressed material 3" unit of Robbins et al. (2019)

am Polygonal shaped mounds ~30–40 km across in similarly shaped depressions; this terrain correlates with the mons terrain Mob of Robbins et al. (2019).

sp Smooth plains cut by networks of linear and curvilinear grooves only in Vulcan Planitia.

cb Closed basin or trench-like linear/curvilinear depressions along the northern edge of Vulcan Planitia.

tr_r Younger dendritic trough set that is linked with closed basins and linear/curvilinear depressions along the northern edge of Vulcan Planitia; this unit was mapped as a radially trending graben system in Beyer et al. (2019; see their Fig. 16).

ct_r Degraded crater that truncates a north-trending arcuate range and is itself filled by ridged materials; the crater rim ridge is locally missing or cut across by troughs that extend across the ridge-bounding valley zone.

ar North-trending arcuate range fronts in the troughed highland terrain (th).

th A highlands terrain that consists of an older set of wide (20–30 km), long (>200–300 km), and deep (3–6 km) troughs that are either terminated at or trend parallel to the north-trending arcuate ranges in this terrain. The ranges are cut across by a younger set of smaller troughs displaying dendritic patterns and terminating at trench-like troughs along the northern rim of Vulcan Planitia.

tr_f Polygonal networks of troughs dominating the troughed highlands terrain (th). Some troughs are truncated by north-trending range-bounding scarps.

cp A highland catered-plain terrain consisting of the oldest group of the degraded craters and polygonal networks of troughs (ct_1).

lr East-trending linear range fronts that bound graben-like basins in the ridge-bounding valley zone (rv) along the southern margin of Oz Terra.

rt Linear ridge terrain characterized by east-trending ridges and ridge-bounding depressions, angular depressions, and angular knobs.

rv Ridge-bounding valley zone expressed by linear scarps and scarp-bounded graben-like valleys.

ct_3 Youngest crater expressed by light-toned radial ejecta rays.

ct_2 Craters with layered ejecta deposits; rampart-like crater morphology.

ct_1 Degraded crater lacking well-preserved ejecta deposits and crater rim ridges.

Figure 1. Geomorphologic map and chronostratigraphy of Charon's encounter hemisphere. (A) Enhanced color view of Charon that combines blue, red and infrared images taken by the New Horizons spacecraft's Ralph/Multispectral Visual Imaging Camera (MVIC) (Moore et al., 2016). (B) A digital elevation model of Charon's encounter hemisphere at a horizontal resolution of 300 m/pixel overlying the Charon New Horizons LORRI MVIC Global Mosaic 300 m v1 (Schenk et al., 2018a). The locations for the topographic profiles shown in Figure 2 are indicated.
(C) Geomorphological map of Charon's encounter hemisphere created in this study. Description of terrain units is listed on the column to the right. (D) The interpreted chronological sequence of the mapped landform units, on the left; possible geological processes responsible for their formation, on the right. Numbers in (D) are the contacts between landform units. See text for detailed description of landform units.

absence of ejecta-apron deposits as noted by Moore et al. (2016). This unit is concentrated in Oz Terra.

Unit *ct*$_2$. This unit has the intermediate-aged and intermediate-sized group of craters that are characterized by layered ejecta-apron deposits, commonly displaying rampart-like morphologies such as those on Mars (cf., Carr et al., 1977; Weiss and Head, 2013). It occurs in both Oz Terra and Vulcan Planitia.

Unit *ct*$_3$. This unit has Charon's youngest-aged and smallest-sized group of craters, characterized by light-toned radial ejecta rays similar to those on the surface of Earth's moon (cf., Morse et al., 2018). This unit is found both in Oz Terra and in Vulcan Planitia.

Unit *rv*. This unit represents ridge-bounding valley zones bounded by linear scarps. The valleys may have a graben-like morphology, their rims bounded by rift-should-like ridges.

Unit *rt*. This is a ridged terrain characterized by linear and parallel ridges. This terrain also exposes polygonal depressions, and angular knobs are scattered locally on the terrain surface.

Unit *lr*. This terrain is characterized by east-trending linear ranges that have scarp-defined range fronts and bound graben-like elongated basins that are mapped as Unit *rv,* as described above. This unit occurs only along the southern margin of Oz Terra directly north of Vulcan Planitia.

Unit *cp*. This unit describes a highland catered-plain terrain in Oz Terra that consists of the oldest, degraded craters (Unit *ct*$_1$) and polygonal networks of troughs, and a highland region bounding the western end of Vulcan Planitia.

Unit *tr*$_1$. This terrain is characterized by polygonal networks of troughs that dominate the landscape of Oz Terra. Note that some troughs in this terrain are truncated by north-trending range-bounding scarps.

Unit *th*. This is a highland terrain that consists of an older set of wide (20–30 km), long (> 200–300 km), and deep (3–6 km) troughs. The troughs are either terminated at or trend parallel to the north-trending arcuate ranges that also occur in this terrain. The arcuate ranges are cut across by a younger set of smaller troughs, which display converging dendritic patterns and terminate locally at trench-like linear depressions along the northern rim of Vulcan Planitia.

Unit *ar*. This unit represents a geomorphological element characterized by north-trending, arcuate range fronts in the troughed highland terrain (Unit *th*).

Unit *ct*$_F$. This unit represents craters whose central uplifts are buried by younger ridged materials. The prototype location is a crater on Oz Terra that shows degraded rim ridges. The same crater truncates a north-trending arcuate range. The crater rim ridge is locally cut across by troughs that extend from the crater-bounding plains to the crater interior.

Unit *tr*$_2$. This unit represents a younger set of dendritic troughs. The troughs are characterized by their termination at closed basins and/or trench-like depressions along the northern edge of Vulcan Planitia. Note that this unit was mapped as a radially trending graben system by Beyer et al. (2019) (see their Fig. 16).

Unit *cb*. This unit denotes closed basins or trench-like linear/curvilinear depressions along the northern edge of Vulcan Planitia. The rims of the basins and trenches are mostly flat, as parts of the bounding plains.

Unit *sp*. This terrain is characterized by smooth plains that are cut by networks of linear and curvilinear grooves in Vulcan Planitia.

Unit *am*. This unit consists of polygonal-shaped mounds that are ~30–40 km across. The mounds are rimmed by similarly shaped moats that have asymmetric profiles: steepening towards the mounds and shallowing towards the bounding plains. This unit occurs only in Vulcan Planitia and was mapped as "the mons terrain" by Robbins et al. (2019).

Unit *fb*. This unit marks a distinctive geomorphological element in Vulcan Planitia, expressed as funnel-like, polygonal-shaped, angular-cornered depressions that have characteristic downward-steepening profiles, their rims displaying cylindrical shapes in their horizontal directions. The angular corners of the depressions exhibit antiformal ridges and synformal grooves. The former were referred to as "broad warps" by Beyer et al. (2019) and Robbins et al. (2019). The funnel-like depressions correlate roughly with the "depressed material 3" unit of Robbins et al. (2019).

Unit *rp*. This is a ridged-plain terrain most clearly observed along the northern margin of Vulcan Planitia. The unit is intermingled with southward-convex, lobate-shaped ridges that are dotted by angular knobs along the ridge crests.

Unit *sf*. This is a smooth-surfaced terrain in Vulcan Planitia that hosts ridges, grooves, and knobs.

Unit *la*$_S$. This unit represents a geomorphological element characterized by its smooth-surfaced, lobate-apron morphology. This type of landform occurs only in the southeastern corner of Oz Terra.

Unit *ln*. This unit consists of parallel linear grooves and ridges exposed on larger planar ridge flanks that bound the northern edge of Vulcan Planitia. The grooves in this terrain are interrupted by smaller knobs within the linear depressions. Some of the linear depressions in this terrain are defined by linked pits. This unit was mapped as "grooves" by Beyer et al. (2019) and "scarp crests" by Robbins et al. (2019).

Unit *rf*. This unit denotes a basin that has a rough-surfaced floor. The rough texture of the basin floor is locally defined by north-trending, evenly spaced ridges. The basin is bounded by a linear scarp in the south and Dorothy crater in the northwest.

Unit *kb*. This unit is characterized by the occurrence of angular to circular knobs, knob trains, and parallel curvilinear ridges.

Unit *la*$_R$. This unit denotes a rough-surfaced, lobate-apron plateau terrain bounded by the largest troughs in Oz Terra. The plateau surface locally displays parallel ridges and furrows trending north and parallel to those exposed in the rough-surfaced terrain (*rf*).

Unit *lb*. This unit occurs along the northern margin of Vulcan Planitia that slopes gently southward. The unit is characterized by lobate ridges locally dotted by angular and circular knobs along ridge crests. The lobate ridges are convex southward in the direc-

tion of the regional slope.

Unit *k*. This unit denotes mappable knobs that have sizes from 1 to 10 km. The knobs exhibit rectangular, polygonal, circular, and oval shapes. The knobs are scattered across Vulcan Planitia but are locally present on Oz Terra. The mapped knobs correlate locally with "the mons unit" of Robbins et al. (2019) in the Vulcan Planitia area.

Unit pt_O and Unit pt_V. These two units are characterized by pitted surfaces in Oz Terra denoted by the subscript "O" and in Vulcan Planitia denoted by the subscript "V". This unit correlates approximately to the "mottled terrain" of Robbins et al. (2019).

Unit *gv*. This unit denotes networks of rill-like grooves exposed in Vulcan Planitia. The grooves show *en echelon* alignments and Y-shaped triple junctions. The groove landform mapped in this study is the same as that described in Moore et al. (2016), Beyer et al. (2019), and Robbins et al. (Robbins et al. (2019).

Unit *ls*. This unit denotes lobate-apron-shaped landforms that occur at the base of linear ridge scarps. These Features were interpreted as landslides by Beddingfield et al. (2019).

4.2 Morphologies and Cross-Cutting Relationships

The most dominant terrain in Oz Terra is the cratered-plain unit (*cp* in Figure 1C), which is the oldest terrain that hosts degraded craters (Unit ct_1) characterized by the lack of clearly defined impact ejecta deposits, central uplifts, and rim ridges. The cratered-plain terrain also hosts polygonal trough networks dominated by north-trending troughs (Unit tr_1). These troughs are ~10 s·km wide, > 100 s·km long, and ~3–5 km in local reliefs against the bounding ranges. The troughs display undulating longitudinal profiles (Figure 2A), U-shaped cross sections, and flat floors (Figure 1B). Note that Figure 2B is severely exaggerated in the vertical direction, with the *V*/*H* ratio = 12 (*V*: vertical; *H*: horizontal). Because of this distortion, the cross section appears to be V-shaped.

The cratered-plain terrain also hosts north-trending, arcuate-shaped ranges that are ~200 km long, 40–60 km wide, and up to ~2 km in the maximum relief (labelled as *'ar'* in Figure 1C). The ranges consistently display steeper eastern flanks, gentler western flanks (Figure 2E), and a westward-concave map-view shape (Figures 1B and 1C).

The polygonal troughs and north-trending arcuate ranges are mapped together as the troughed highland terrain (Unit *th* in Figure 1C), locally overlain by a knobbed terrain (Unit *kb* in Figure 1C) that consists of linear and curvilinear ridges, linear and curvilinear knob trains, and patches of scattered pits (labelled as 'pt_O' in Figure 1C). Figure 3A shows key morphological features and their spatiotemporal relationships in the troughed highland terrain (*th*). In this image, east-facing scarps (Feature 1a) bounding the north-trending arcuate ranges have longer, gentler west-sloping flanks (Feature 2) and shorter, steeper eastern range flanks. Note that the ranges are separated by parallel northwest-trending troughs (Feature 3a in Figure 3A). An arcuate range front (Feature 1b in Figure 3A) truncates both crater rims (Feature 4 in Figure 3A) and an older set of east-trending troughs (Feature 5 in Figure 3A). The north-trending ranges themselves are crosscut by a younger dendritic network of troughs (Feature 6 in Figure 3A). The ranges are also truncated (see Feature 1b in Figure 3A) by a younger crater (Feature 7 in Figure 3A) filled by a ridged-plain material. A degraded crater with a dark-material apron (Feature 8 in Figure 3A) is crosscut by an east-trending trough (Feature 3b in Figure 3A).

Figure 3B is a zoom-in view of an east-facing scarp zone shown in Figure 3A, which consists of a single scarp trace in the south (Feature 1a) and multiple scarp traces (Features 1b and 1c) in the north. The scarp zone truncates craters (e.g., Features 2 in Figure 3B) and troughs (Feature 3 in Figure 3B), but the zone itself is crosscut by younger craters (e.g., Features 4 in Figure 3B) and superposed by a younger dendritic trough system (Feature 5). The scarp-bounded range crest displays a set of range-front-parallel

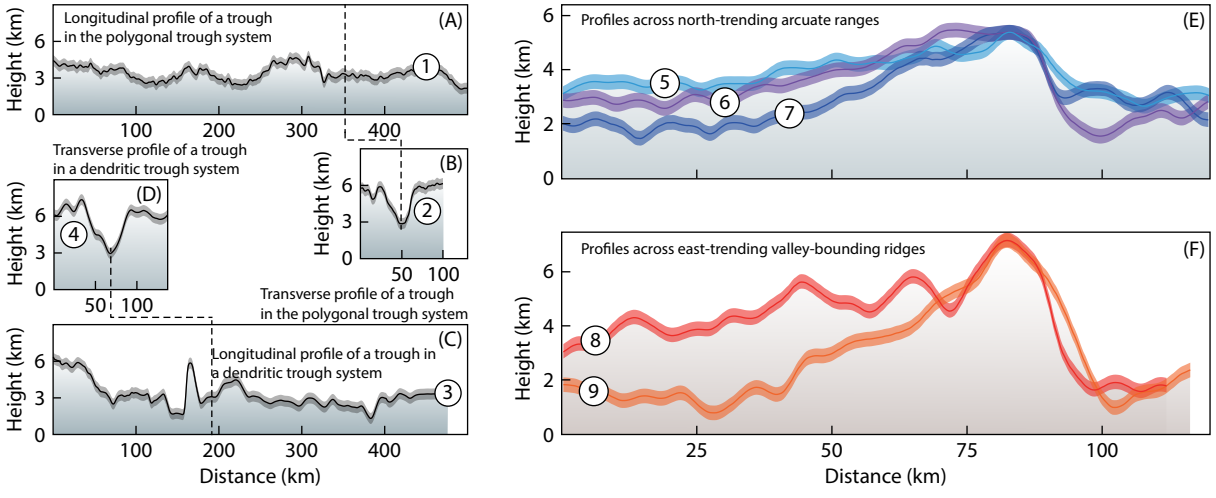

Figure 2. Topographic profiles of ranges, ridges, and troughs. (A) Longitudinal and (B) transverse profiles of a linear trough in the polygonal trough network (Unit tr_1). (C) Longitudinal and (D) transverse profiles of a curvilinear trough in a dendritic trough network (Unit tr_2). (E) Topographic profiles across north-trending arcuate ranges. (F) Topographic profiles across ridges in the eastern ridge-bounding valley zone (Unit *rv*). The widths of the topographic profile lines represent the uncertainties quoted from Schenk et al. (2018a). Digital elevation model data are from Schenk et al. (2018a).

ridges (Feature 6 in Figure 3B). The scarp-bounded west-sloping range flank is draped over by a younger crater surrounded by proximal darker-toned and distal lighter-toned ejecta deposits (Feature 7 in Figure 3B).

The arcuate ranges (Feature *ar* in Figure 1C) are locally cut across by east-trending and westward-converging dendritic networks of troughs (Unit tr_2) (Figure 3C), which are shorter and narrower than the orthogonal troughs mapped as Unit tr_1. Note that in Figure 3C, the dendritic network of troughs (Unit tr_2) exhibits hanging-valley morphologies (Feature 1) and terrace-rise-like scarps (Features 2a–2c) along the margin of a meandered, steep-walled trough (Feature 3). However, like polygonal troughs, the trunk channel of the dendritic troughs tr_2 displays undulating longitudinal profiles (Figure 2C) and U-shaped cross sections when the vertical exaggeration shown in Figure 2D is removed.

The north-trending arcuate ranges (Unit *ar* in Figures 1C and 1D),

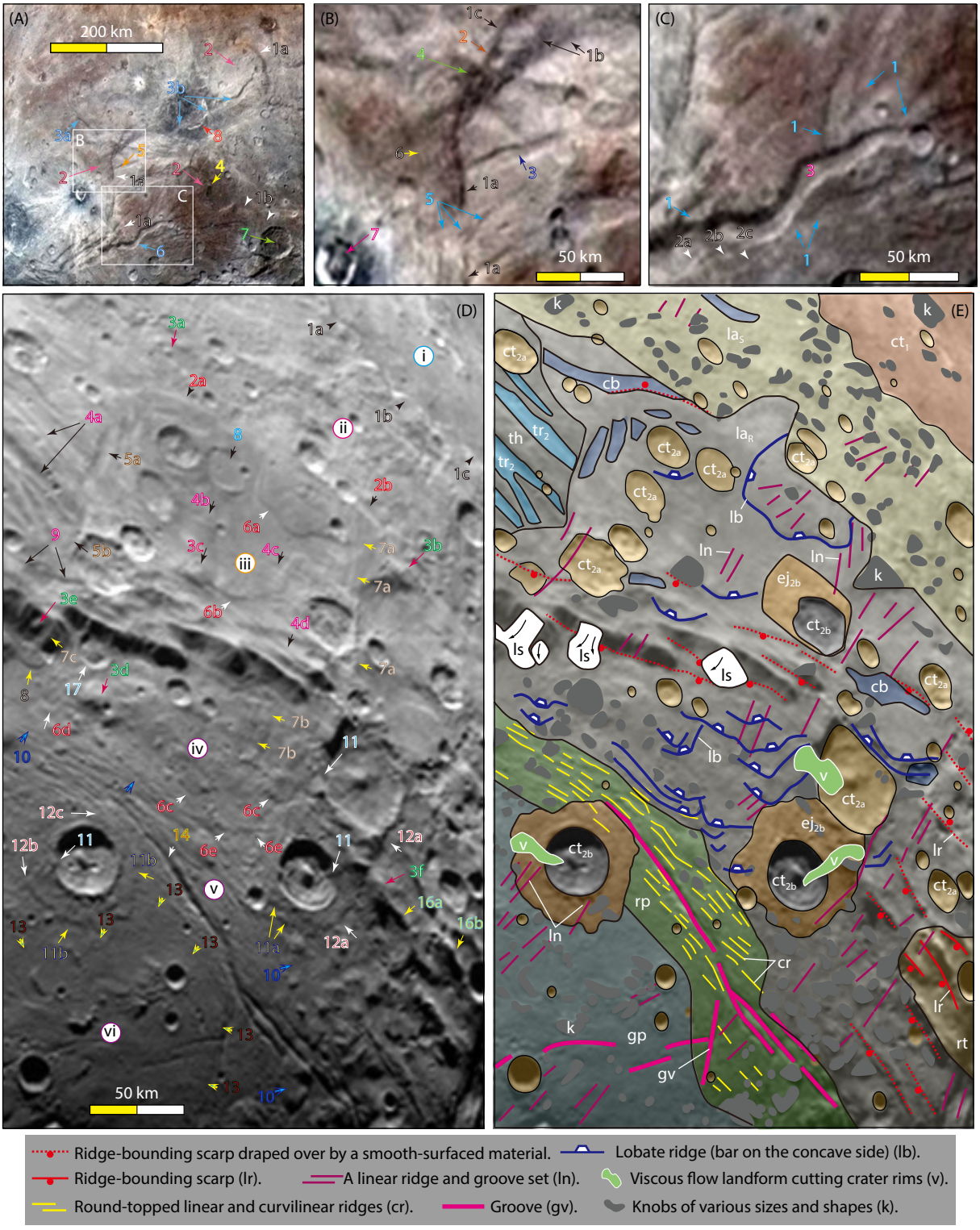

Figure 3. Morphological associations of the mapped landform units. (A) Key morphological features and their spatiotemporal relationships in the troughed highland terrain (*th*). East-facing scarps (Feature 1a) bounding north-trending ranges that have longer west-sloping flanks (Feature 2) and shorter eastern range flanks. The ranges are separated by parallel north-trending troughs (Feature 3a). An arcuate range front (1b) truncates both crater rims (Feature 4) and an older set of east-trending troughs (Feature 5). The north-trending ranges themselves are crosscut by a younger dendritic network of troughs (Feature 6). The ranges are also truncated (see Feature 1b) by a younger crater (Feature 7) filled by a ridged-plain material. A degraded crater with a dark-material apron (Feature 8) is crosscut by an east-trending trough (Feature 3b). (B) A zoom-in view of an east-facing scarp zone that consists of a single scarp trace in the south (Feature 1a) and multiple scarp traces (Features 1b and 1c) in the north. The scarp zone truncates a crater (Features 2) and troughs (Feature 3), but the zone itself is crosscut by younger craters (e.g. Features 4) and superposed over by a younger dendritic trough system (Feature 5). The scarp-bounded range crest displays a set of range-front-parallel ridges (Feature 6). The scarp-bounded west-sloping range flank is draped over by a younger crater surrounded by proximal darker-toned and distal lighter-toned ejecta deposits (Feature 7). (C) A zoom-in view of a dendritic network of troughs (tr_2) that exhibits hanging-valley morphologies (Feature 1) and terrace-rise-like scarps (Features 2a–2c) along the margin of a meandered, steep-walled trough (Feature 3). (D) Key landforms across the topographic boundary zone between Oz Terra and Vulcan Planitia. Dorothy crater (Feature *i*) is characterized by a smooth-surfaced basin floor and lies next to the rough-surfaced lobate-apron terrain (la_R) on Oz Terra (Feature *ii*). The smooth-surface lobate-apron terrain (Feature *iii*) extends from Oz Terra to Vulcan Planitia (Feature *iv*). Features 1a–1c mark the contact between Dorothy crater and Unit la_R, whereas Features 2a and 2b mark the contact between Unit la_R and the smooth-surfaced lobate-apron terrain (Unit la_S and Feature *iii*). Features 3a–3b are examples of mapped knobs in Unit la_R, which are up to > 20 km in the longest dimension. Features 3c and 3d are examples of knobs mapped in Unit la_S, which have smoother surfaces than those in Unit la_R (cf. Feature 3b). Note that a knob is draped over a south-facing scarp (Feature 3e). Feature 4a marks a zone of northwest-trending linear troughs, mapped as Unit tr_2, that are crosscut by a northeast-trending linear depression (Feature 5a) and a similarly trending scarp (Feature 5b). The troughs (tr_2) and their bounding walls are draped over by Unit la_S (Features 4b–4d). Unit la_S hosts south-convex lobate aprons (Features 6a, 6b and 6c), south-convex lobate ridges (Features 6d and 6e), north-trending linear ridges and grooves (Features 7a and 7b), and craters filled by flat smooth-surfaced materials (Feature 8; also see description of this same feature in Robbins et al., 2019). A north-trending ridge (Feature 7c on the left-central edge of the image) exposed on the surface of a south-facing scarp terminates downward at a lobate apron (Feature 8). The lack of a corresponding breakaway topographic feature rules out the possibility that the apron landform could be a landslide. Feature 9 shows a possible degraded crater cut by a south-facing scarp, which likely represents the trace of a normal fault. Feature 10 represents the contact between the smooth-surfaced lobate-apron unit (Features *iii* and *iv*) and the ridged plain terrain (Feature *v*). Feature 11 describes flow-like features that cut across crater rims and extend into the crater-basin floors. Layered impact deposits for one crater are deformed by northwest-trending ridges (Feature 11a), whereas layered impact deposits for another crater (Feature 11b) are truncated (Feature 12b) and overprinted (Feature 12c) by a zone of parallel ridges (*cr*) in the ridged plains terrain (*rp*). The boundary between ridged-plain terrain (*rp* and Feature *v*) and the smooth-surfaced lobate-apron terrain (Unit la_S and Feature *vi*) is transitional (see Feature 13). This contact is crosscut by younger grooves (Feature 14). In the southwestern corner of the image, northwest-trending smooth-surfaced linear ridges (Feature 16a) are locally superposed by knobs (Feature 3f). In contrast, ridges with the same trend directly to the southeast display rougher surfaces (Feature 16b). A partially filled crater lies at the base of a range bounding scarp (Feature 17). (E) A geomorphological map that summarizes all the aforementioned landforms shown in (D). Abbreviated map symbols are: *k*, knobs; *ln*, sets of linear ridges and grooves; *v*, viscous flow features cutting across crater-rim ridges and extending into crater basin floors; *cr*, sets of parallel linear and curvilinear ridges; *gv*, grooves; and *lr*, linear ridge. All other landform units are defined in Figure 1. Note that the geomorphological features superposed by the smooth-surfaced lobate-apron unit, such as the east-trending scarps and northwest-trending ridges, are shown by dashed lines.

locally crosscut by younger craters (ct_F in Figures 1C and 1D), are terminated by the east-trending ridge-bounding valley zone (Unit *rv* in Figures 1C and 1D). The truncated arcuate ranges do not cut across the valley zone, but an arcuate range south of the valley zone is present along the western end of Vulcan Planitia (Feature 1 in Figure 1B). The right-lateral offset of two north-trending ranges north (Feature 2 in Figure 1B) and south (Feature 1 in Figure 1B) of the valley zone is ~400 km.

Valleys in the eastern segment of the valley zone (Unit *rv*) are bounded by rift-shoulder-like rim ridges (Feature 3 in Figure 1B). The ridges change trending direction from northeast (Feature 4 in Figure 1B) to northwest (Feature 5 in Figure 1B) around the north-eastern corner of Vulcan Planitia. In contrast, valleys in the western segment of the valley zone (Unit *rv*) are bounded by plains without rim ridges (Feature 6 in Figure 1B; cf., Feature 3 in Figure 1B). Note that the topographic profiles of the valley-bounding, east-trending ridges differ from those of the north-trending, arcuate ranges in that the former have higher reliefs and steeper range fronts (Figures 2E and 2F).

The oldest smooth-plain terrain (Unit *sp* in Figure 1C) is dotted by isolated knobs (Feature '*k*' in Figure 1C), polygonal-shaped mounds (Unit *am* in Figure 1C), funnel-like depressions (Unit *fb* in Figure 1C), variously shaped pits (Unit pt_V in Figure 1C), and craters surrounded by layered ejecta deposits (Unit ct_2 in Figure 1C). The largest funnel-like depression (~70 km in the longest dimension) with a triangular map-view shape (Feature 7 in Figure 1B) occurs in the topographic transition zone between the eastern edge of Vulcan Planitia and western margin of the linear ridge terrain (Unit *rt* in Figure 1C). The smooth plains terrain is crosscut by northwest-trending ridges (labelled as '*cr*' Figure 1C) hosted by the ridged plains terrain (Unit *rp* in Figure 1C). The ridges are in turn truncated by the smooth-surfaced lobate-apron terrain (Unit la_S in Figure 1C), which is crosscut by the youngest rough-surfaced terrain (Unit la_R in Figure 1C). Unit la_R itself defines a lobate-shaped plateau (Figure 3E; also see Feature 8 in Figure 1B). The plateau terrain differs from arcuate ranges (i.e., Feature '*ar*' in

Figure 1C) in that its surface lacks troughs.

Figure 3D displays key landforms across the topographic boundary zone between Oz Terra and Vulcan Planitia. Dorothy crater in the northeastern part of the image (Feature *i*) is characterized by a smooth-surfaced basin floor and lies next to the rough-surfaced lobate-apron terrain (la_R) on Oz Terra (Feature *ii*). The smooth-surface lobate-apron terrain (Feature *iii*) extends from Oz Terra to Vulcan Planitia (Feature *iv*). Features 1a–1c in Figure 3D mark the contact between Dorothy crater and Unit la_R, whereas Features 2a and 2b in Figure 3D mark the contact between unit la_R and the smooth-surfaced lobate-apron terrain (Unit la_S and Feature *iii*). Features 3a–3b in Figure 3D are examples of mapped knobs in Unit la_R, which range up to > 20 km in the longest dimension, whereas Features 3c and 3d in Figure 3D are examples of knobs mapped in Unit la_S with smoother surfaces than those in Unit la_R (cf. Feature 3b in Figure 3D). Note that a knob is draped over a south-facing scarp (Feature 3e in Figure 3D). Feature 4a in Figure 3D marks a zone of northwest-trending linear troughs mapped as Unit tr_2 that are crosscut by a northeast-trending linear depression (Feature 5a in Figure 3D) and a similarly trending scarp (Feature 5b in Figure 3D). The troughs (Unit tr_2) and their bounding walls are draped over by Unit la_S (Features 4b–4d in Figure 3D). Unit la_S hosts south-convex lobate aprons (Features 6a, 6b and 6c in Figure 3D), south-convex lobate ridges (Features 6d and 6e), north-trending linear ridges and grooves (Features 7a and 7b in Figure 3D), and craters filled by flat smooth-surfaced materials (Feature 8 in Figure 3D; also see description of this same feature in Robbins et al., 2019). A north-trending ridge (Feature 7c on the left-central edge of the image in Figure 3D) exposed on the surface of a south-facing scarp terminates downward at a lobate apron (Feature 8 in Figure 3D). The lack of a corresponding breakaway topographic feature rules out the apron landform to be a landslide. Feature 9 in Figure 3D shows a possible degraded crater cut by a south-facing scarp, which likely represents the trace of a normal fault. Feature 10 in Figure 3D represents the contact between the smooth-surfaced lobate-apron unit (Features *iii* and *iv* in Figure 3D) and the ridged plain terrain (Feature *v* in Figure 3D).

Feature 11 in Figure 3D describes flow-like landforms that cut across crater rims and extend into the crater-basin floors. Layered impact deposits for one crater are deformed by northwest-trending ridges (Feature 11a in Figure 3D), whereas layered impact deposits for another crater (Feature 11b in Figure 3D) are truncated (Feature 12b in Figure 3D) and overprinted (Feature 12c in Figure 3D) by a zone of parallel ridges (*cr*) in the ridged plains terrain (*rp*). The boundary between ridged-plain terrain (*rp* and Feature *v*) and the smooth-surfaced lobate-apron terrain (Unit la_S and Feature *vi*) is transitional (see Feature 13 in Figure 3D). This contact is crosscut by younger grooves (Feature 14 in Figure 3D). In the southwestern corner of the image, northwest-trending smooth-surfaced linear ridges (Feature 16a in Figure 3D) are locally superposed by knobs (Feature 3f in Figure 3D). In contrast, ridges with the same trend directly to the southeast display rougher surfaces (Feature 16b in Figure 3D). A partially filled crater lies at the base of a range bounding scarp (Feature 17 in Figure 3D).

The geomorphological relationships described above are summarized in the geomorphologic map shown in Figure 3E. Within the four younger units that are superposed over the eastern valley zone (*vz* in Figure 3E), we note that (1) all lobate-apron landforms are convex southward, (2) craters with layered ejecta deposits have their rims locally breached and floors partially filled by viscous-flow materials (labelled as '*v*' in Figure 3E), and (3) layered ejecta deposits are locally superposed by ridges (labelled as '*cr*' in Figure 1C) that are crosscut by younger polygonal networks of grooves (labelled as '*gv*' in Figure 1C). Note that all other units shown in Figure 3E are defined in Figure 1C.

4.3 Degraded Craters

Craters mapped as Unit ct_1 and Unit ct_2 display variably degraded morphologies (Figures 4 and 5). The post-cratering modification is expressed by partial breaching of crater rims, partial infilling of crater basins, and superposition of grooved, ridged, hummocky-textured, and smooth-surfaced materials as detailed below.

Figure 4A shows a crater with a partially preserved rim ridge marked as Feature 1 along its northern and southern edges. In contrast, the western and eastern rims of the same crater are bounded by flat plains where the rim ridge is missing (Feature 2). The crater basin is cut across by a series of northwest-trending ridges and grooves (Feature 3), and the crater floor and crater-bounding plains share the same hummocky surface texture. The latter relationship requires a post-cratering resurfacing process that created the shared surface morphology. To the southeast of the crater mentioned above is a smaller crater that is partially superposed by a linear ridge that cuts across its rim (Feature 4 in Figure 4A; also see details in Figure 4B).

Figure 4B shows a crater with its western rim ridge breached and cut across by an east-trending knob train (Feature 1). Parallel east-trending ridges are also present on the crater floor (Feature 2). A central mound is present on the crater floor (Feature 3).

Figure 4C shows a crater whose western and eastern rims are superposed by east-trending ridges and grooves (Features 1 and 2). A wider ridge cutting across the crater rim has a dumbbell shape characterized by the occurrence of higher mounds at the two ends (Feature 3).

Figure 4D shows a zoom-in view of the smaller crater shown in Figure 4A. The crater rim is breached in three places (Features 1, 2, and 3), which are expressed by the superposition of 2–5 km wide linear grooves over the crater edge. The crater floor displays curvilinear ridges that terminate at the ends of the crater-rim-cutting grooves (Feature 4).

Figure 4E shows a crater that is breached by northeast-trending grooves and ridges across its western and eastern rims (Features 1 and 2). The crater floor displays a central uplift with a well-defined peak (Feature 3).

Figure 4F shows a crater with its western rim superposed by an east-trending, 8–12-km wide, > 30 km long ridge (Feature 1). The flat top of the ridge is superposed by narrower ridges that are parallel to the general trend of the bigger, hosting ridge (Feature 2). The wider ridge splits into two branches as it enters the crater floor (Features 3a and 3b).

Figure 4G shows a sheet-like landform that is superposed over the

northwestern rim of a crater (Feature 1). The sheet-like landform partially enters the crater basin (Feature 2); its abrupt termination margin appears to have been sourced from a smaller, rampart-style impact crater from the west (Feature 3).

Figure 4H shows a crater that has a central peak and ring-shaped ridges and grooves on the crater floor. The crater's eastern rim (Feature 1) and western rim (Feature 2) are draped over by younger ridges. The eastern ridge originates from a mound and narrows as it extends into the crater floor.

Figure 4I shows another crater that has a central uplift and well-preserved northern and southern rim ridges. However, its eastern rim (Feature 1) and western rim (Feature 2) are breached by ~7-km wide, round-topped ridges that extend into the interior of the crater floor.

Figure 4J shows an east-trending ridge system that cuts across a quasi-triangular-shaped crater, whereas Figure 4K shows a circular depression (Feature 1) with a smooth and flat floor that may represent a partially filled crater basin. Note that in Figure 4K, Feature 2 denotes a circular-rim ridge that bounds a discontinuous circular groove. The latter appears to be relics of a filled crater.

Figures 4L and 4M show a DEM image of Schenk et al. (2018a) along with a corresponding optical image from the same area. In both images, Features 1, 2, and 3 mark linear depressions that cut across the crater rim. In the same images, Feature 4 denotes a tongue-shaped landform superposed over the crater wall and partially the crater floor.

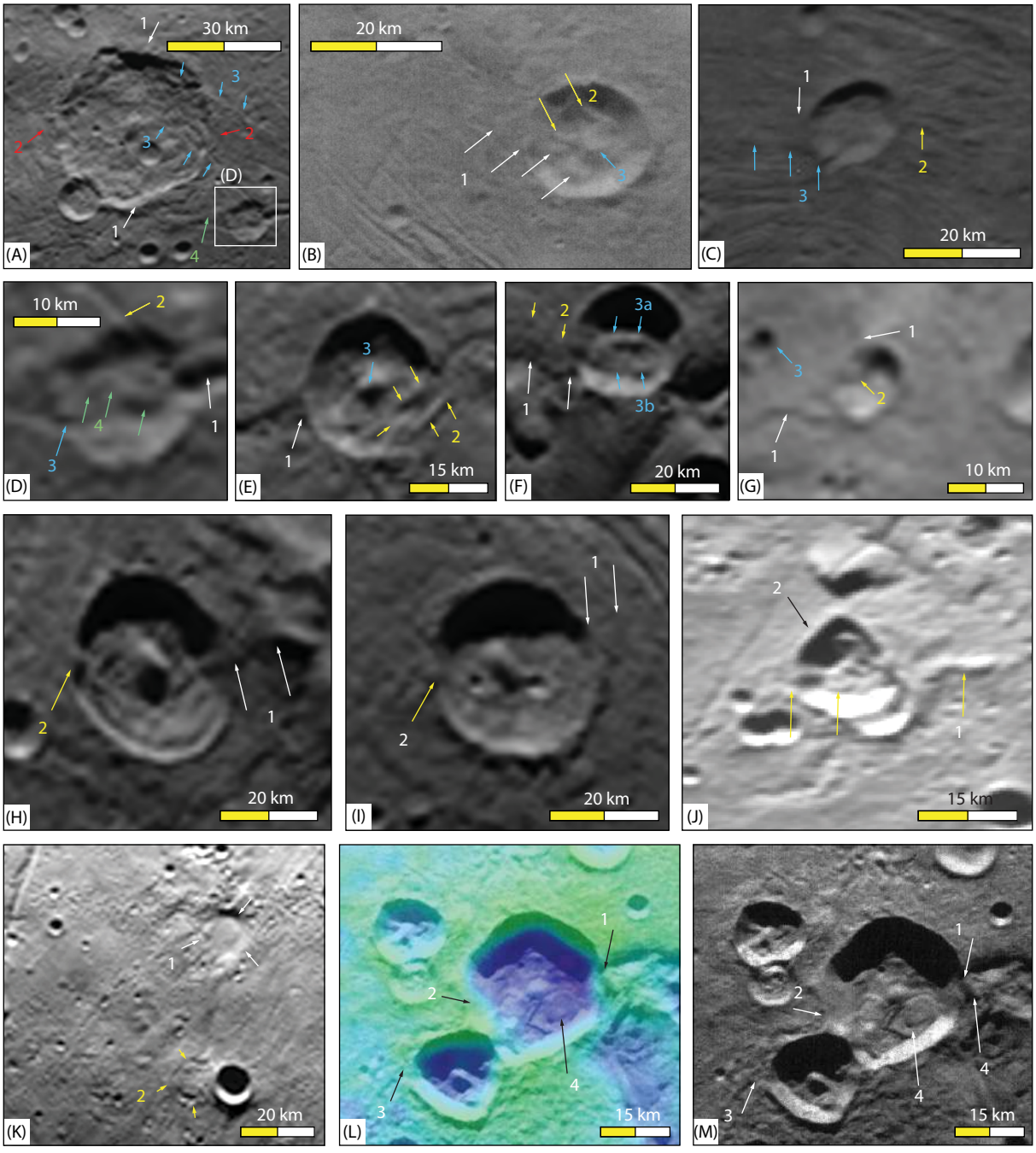

Figure 4. Modified craters in Vulcan Planitia. (A) A crater with a partially preserved rim ridge marked as Feature 1 along its northern and southern edges. In contrast, its western and eastern rims are bounded by flat plains where the rim ridge is missing (Feature 2). The impact basin is cut across by a series of northwest trending ridges and grooves (Feature 3). The crater floor and crater-bounding plains share the same hummocky surface texture, which requires a post-cratering resurfacing process to create such a textured surfaced (image ID mp1_0299180334_0x530_sci at a resolution of 622 m/pixel). (B) A crater with its western rim ridge breached and draped over by an 8–10 km wide gentle-sloped, smooth-surfaced material (Feature 1). Parallel east-trending ridges (Feature 2) and central mound (Feature 3) are present on the crater floor (image ID lor_0299180418_0x630_sci_3 at a resolution of 154 m/pixel). (C) A crater with its western and eastern rims superposed by 8-10 km wide grooved materials (Features 1 and 2). A wider ridge characterized by the occurrence of higher mounds at two ends cut across the crater rim (Feature 3) (lor_0299175682_0x630_sci_4 at a resolution of 410 m/pixel). (D) A zoom-in view of the smaller crater shown in (A). The crater rim is breached in three places (Features 1, 2, and 3) by 2–5 km wide grooves. The crater floor displays curvilinear ridges that terminate at the ends of the crater-rim-cutting grooves (image ID mp1_0299180334_0x530_sci at a resolution of 622 m/pixel). (E) A crater is breached by grooves and ridges across its western and eastern rims (Feature 1 and 2). The crater floor displays a well-defined central peak (Feature 3) (image ID mp1_0299180334_0x530_sci at a resolution of 622 m/pixel). (F) A crater with its western rim superposed by an 8–12-km wide, hummocky-surface material (Feature 1). The flat top of the ridge is superposed by narrow ridges that are parallel to the general trend of the hosting ridge (Feature 2). The hosting ridge splits into two branches as it enters the crater floor (Feature 3a and 3b) (image ID mp1_0299180334_0x530_sci at a resolution of 622 m/pixel). (G) A crater that is partially filled by a sheet-like smooth-surfaced material with lobate-shaped scarps (Feature 1 and 2). The sheet-like landform appears to have been sourced from a smaller, rampart style impact crater from the west (Feature 3) (image ID mp1_0299180334_0x530_sci at a resolution of 622 m/pixel). (H) A complex crater with its eastern rim (Feature 1) and western rim (Feature 2) draped over by ridges (image ID mp1_0299180334_0x530_sci at a resolution of 622 m/pixel). (I) A crater with its eastern rim (Feature 1) and western rim (Feature 2) breached and draped over by 7-km wide round-topped ridges (image ID mp1_0299180334_0x530_sci at a resolution of 622 m/pixel). (J) An east-trending ridge system, superposed over a quasi-triangular-shaped crater. Image is cropped from the Charon New Horizons LORRI MVIC Global Mosaic 300 m v1 created by Schenk et al. (2018a). (K) Feature 1 shows a circular depression with a smooth floor that may represent a partially filled crater basin. Feature 2 shows a circular rim ridge and a circular groove, which could be the relics of a filled crater. (Image ID lor_0299180424_0x630_sci_3 at a resolution of 622 m/pixel). (L) An image cropped from the global digital elevation model of Schenk et al. (2018a) at a resolution of 300 m/pixel, and (M) an image of the same area cropped from a larger image with the identification number of ID lor_0299180421_0x630_sci_3 at a resolution of 154 m/pixel. In both images, Features 1, 2, and 3 indicate the locations where crater rims are breached by linear depressions, and Feature 4 shows a tongue-shaped material that is superposed over the crater wall and the crater floor.

Figures 5A–5B show a crater with its southern margin (Feature 1) breached and crosscut by a series of northeast-trending ridges (Feature 2) along a gap between the rim ridges. Figures 5C–5D show a crater (Feature 1) with its southwestern margin buried by a younger sheet-like landform (Feature 2). The same images also show a partially preserved semi-circular ridge (Feature 3) that bounds a flat-floored circular basin (Feature 4). Note that the rim ridge of the basin is breached in the northeast (Feature 5). The circular shaped basin (Feature 4) could have originated from an impact; its flat floor and the breached rim ridge require the crater to have been degraded by post-impact processes.

Figures 5C–5D show a semi-circular ridge (Feature 6) bounding a quasi-circular depression (Feature 7) with a complex floor morphology due to the presence of superposed impact craters (Feature c). Note that the circular basin marked as Feature 7 does not have the northeastern rim, which is occupied by a plain connecting with the basin floor (Feature 8). Note that a southwest-pointing lobate ridge (Feature 9) cuts across the northeastern rim of a smaller crater. Distinctive landforms are also displayed in Figures 5C and 5D. These include arête-like ridges (Feature A), dendritic network of troughs (Feature D), hanging-valley-like landforms (H), flat-topped lobate aprons (Feature LA), pyramid-like peaks (Feature P), and U-shaped valleys (Feature U).

The superposed post-cratering landforms in Figures 4 and 5 are typically 5–10 km in dimension. This observation implies that craters older than the superposed landforms and smaller than 5–10 km in size could have been completely or partially buried. On the other hand, craters larger than 5–10 km in size would have been better preserved on the surface of Charon.

4.4 Chronological Sequence of Landform Units

The sequence of geologic events revealed by the cross-cutting relationships discussed above (see also Figure 1D) can be summarized as the following contact relationships, numbered from oldest to youngest in age for clarity:

Contact 1. The Vulcan Planitia basin (not its surficial deposits) is interpreted to be the oldest geomorphological feature, because its margins represented by the ridge-bounding valley zone (Unit *rv*) and linear-ridge terrain (Unit *lr*) are crosscut and/or superposed by all other mapped landform units.

Contact 2. The troughed highland terrain (Unit *th*) featuring north-trending arcuate ranges (Unit *ar*) is superposed on top of the cratered-plain terrain (Unit *cp*), older troughs (Unit tr_1), and degraded craters (Unit ct_1) that lack ejecta aprons and display partially preserved crater rims.

Contact 3. The north-trending arcuate ranges (Unit *ar*) are crosscut by a crater (Unit ct_F) with the locally breached rim ridge, younger dendritic troughs (Unit tr_1), and younger elongated trench-like depressions (Unit *cb*) bounded by the smooth plains terrain (Unit *sp*) hosting polygonal-shaped mounds (Unit *am*), funnel-like basins (Unit *fb*), and knobs of various shapes and sizes (Unit *k*).

Contact 4. Parallel linear and curvilinear ridges (Unit *cr*) in the ridged plains terrain (Unit *rp*) cut across the smooth plains terrain (Unit *sp*).

Contact 5. Smooth-surfaced terrains with (Unit la_S) or without (Unit *sf*) lobate landforms are superposed over the ridged plains terrain (Unit *rp*).

Contact 6. A rough-floored basin terrain cuts across the linear-ridge terrain (Unit *lr*) and the smooth-surfaced lobate-apron terrain (Unit la_S).

Contact 7. The rough-surfaced lobate-apron terrain (Unit la_R) truncates landforms in Unit la_S.

Contact 8a. The pitted terrain in Oz Terra (Unit pt_O) is superposed over the knobbed terrain (*kb*) interpreted to be coeval with Unit la_R based on their similar surface textures (i.e., dotted knobs, curvilinear ridges, and the absence of troughs).

Contact 8b. The pitted terrain in Vulcan Planitia (Unit pt_V) is superposed over the smooth-surfaced plains terrain (Unit *sp*), which is the oldest terrain of a series of landform units (i.e., *sp, rp,* la_S, and la_R) that are emplaced sequentially from south to north over the topographic boundary between Oz Terra and Vulcan Planitia.

Contact 9. Lobate-shaped landforms at the base of scarp-bounded ridges and networks of grooves that crosscut the smooth-surfaced plains (Unit *sp*) and ridged plains (Unit *rp*). Note

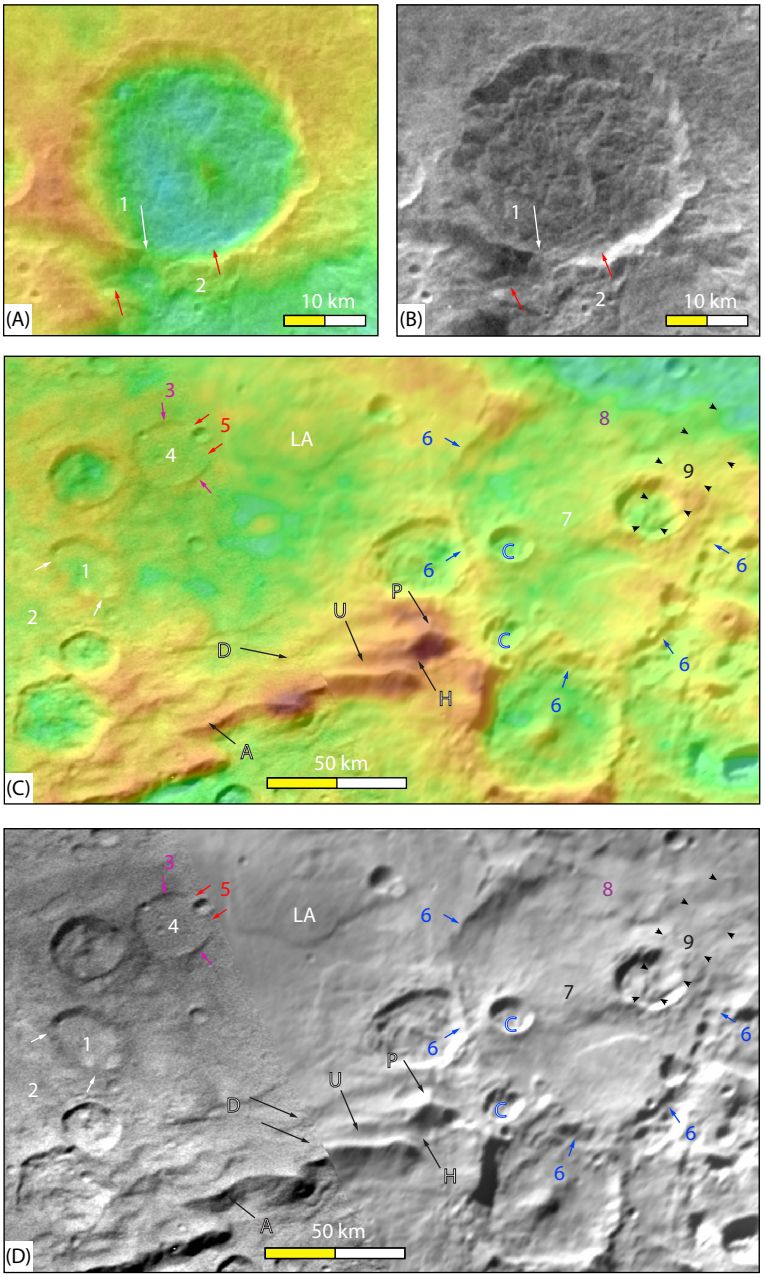

Figure 5. Modified craters in Oz Terra. (A)–(B) An image cropped from the global digital elevation model of Schenk et al. (2018a) at a resolution of 300 m/pixel (A), and an image of the same area cropped from a larger image with the identification number of ID lor_0299180412_0x630_sci_3 at a resolution of 154 m/pixel (B). (C)–D) An image cropped from the global digital elevation model of Schenk et al. (2018a) at a resolution of 300 m/pixel (C), and an image cropped from the Charon New Horizons LORRI MVIC Global Mosaic 300 m v1 (Schenk et al., 2018a) (D).

that northwest-trending linear grooves and ridges (Unit *ln*), southward-convex lobate ridges and lobate aprons (Unit *lb*), and knobs (Unit *k*) are scattered across Vulcan Planitia.

5. Discussion

5.1 Testing Existing Models for the Geomorphologic Development of Charon

Any models for the tectonic and landscape evolution of Charon must explain the following observations:

(1) the absence of ejecta deposits around the largest impact craters (Moore et al., 2016),
(2) partial or complete removal of crater rim ridges of the same largest craters (i.e., Unit ct_1 in Figure 1C; cf. Figure 1B) (also see Moore et al., 2016),
(3) extensive modification of craters for larger craters mapped as Units ct_1 and ct_2 by superposition of younger landforms across the crater rims and crater floors and erosional removal of crater rim ridges expressed by crosscutting grooves (Figures 3D, 3E, 4, and 5),
(4) truncation and omission of impact craters and crater rim ridges of craters along the eastern edges of the north-trending arcuate ranges in Oz Terra (Figures 3C, 10A, and 10C),
(5) localization of extension along the northern rim of Vulcan Planitia (Moore et al., 2016; Desch and Neveu, 2017),
(6) first-order troughs (i.e., generally > 30 km in width) in Oz Terra that are mutually terminating/crosscutting and orthogonally trending north and east (Figures 1B and 1C) (Moore et al., 2016),
(7) second-order dendritic troughs (generally < ~20 km in width) that display hanging valley morphologies at the trough intersections (Figures 3C, 6A, and 6C),
(8) water-ice lobate ridges and lobate aprons (Figures 3D, 8A, and 8E),
(9) parallel and curvilinear round-topped ridges along the northernmost part of Vulcan Planitia (Figures 3D and 3E), and
(10) scattered blocks of various sizes with or without moated margins across Vulcan Planitia.

An ad hoc model may explain one of the above observations. For example, the infilling of crater basins as shown in Figures 3D–3E, 4 and 5 may be explained by the early proposed cryovolcanism (Moore et al., 2016; Beyer et al., 2019). Although the lack of central- or fissure-style volcanic constructs and the absence of tube-shaped elongated landforms (Moore et al., 2016; Beyer et al., 2019; this study) preclude an extrusive style of cryovolcanism, these observations do not rule out buried cryolava-feeder systems below Vulcan Planitia. Subsurface magmatic plumbing has been inferred for the emplacement of lunar flood basalts (e.g., Andrews-Hanna et al., 2013; Head and Wilson, 2017), which could serve as an analogue for the proposed cryovolcanism in the existing literature (Beyer et al., 2019). Regardless of the style of emplacement, cryovolcanism alone is incapable of explaining the other crater-modification observations such as the absence of impact ejecta deposits and partial or complete removal of rim ridges of the largest craters on Charon's encountered hemisphere (Moore et al., 2016).

The tectonic history of Charon has been inferred from various thermo-mechanical models based on different initial and boundary conditions. In a hot-start model, Rhoden et al. (2020) showed that extensional fractures with longitudinally varying trends could form in the polar and equatorial regions if Charon had an eccentric orbit and a subsurface ocean. The east–west-trending fractures at mid-latitudes predicted by this model are inconsistent with the east-trending extensional belt of Moore et al. (2016) and Desch and Neveu (2017) in the equatorial region (Figures 1B and 1C).

In an alternative hot-start model, the east-trending extensional belt and troughs of various sizes across Oz Terra are interpreted to have been formed by subsurface ocean freezing (Moore et al., 2016; Desch and Neveu, 2017; Spencer et al., 2021). This interpretation requires an isotropic tensile stress field, which does not explain the localized east-trending extensional belt along the boundary between Oz Terra and Vulcan Planitia. It also does not explain the truncation and omission of craters along the eastern edges of north-trending, eastward-convex arcuate ranges.

Assuming a cold start, Malamud et al. (2017) formulated a one-dimensional thermo-mechanical model that is capable of tracking the evolution of Charon's radius, which in turn predicts its global extension vs. contraction history. Their model considers the effect of compaction of initially porous ice–rock mixtures by self-gravitation, ice–water differentiation through two-phase flow, and heating/cooling due to hydration/dehydration of silicate minerals. Malamud et al. (2017) showed in their model that amorphous ice in the top 10 km of Charon would remain unprocessed in the entire history of Charon. Meanwhile, their model predicts early (0–165 Ma) global contraction with the fastest rate at ~140–165 Ma, subsequent global expansion at ~165–450 Ma, followed by a constant radius until ~1 Ga, and final global contraction after ~1 Ga. Similar to the ocean-freezing model of (Beyer et al., 2019), the thermo-mechanical model of Malamud et al. (2017) predicts isotropic compressive or extensional stress fields. Such stress states do not explain the localization of the east-striking extensional belt.

Although the lowland region of Vulcan Planitia has been regarded as a site of cryovolcanism (Beyer et al., 2019), we are unable to identify features resembling cryovolcanic constructs such as those interpreted on Titan (Lopes et al., 2007) and Pluto (Schenk et al., 2018b; Cruikshank et al., 2019; Martin and Binzel, 2021; Singer et al., 2022). We are also unable to identify fissure-type eruption centers such as the tiger-stripe fractures on Enceladus (Spencer et al., 2009; Yin and Pappalardo, 2015; Helfenstein and Porco, 2015). Any volcanic conduits responsible for the accumulation of the interpreted cryolavas in Vulcan Planitia must be buried below the surface.

As mentioned above, our mapping does not duplicate the early efforts of crater mapping by Robbins et al. (2017), Singer et al. (2019), and Robbins and Singer (2021). Rather, our mapping focuses on the type of cratering and their relationships to the surrounding landforms. To this end, we have identified three types of craters mapped as Unit ct_1, Unit ct_2 and Unit ct_3 in Figure 1C. Unit ct_1 represents the oldest craters with diameters $D > 50$ km. They occur exclusively on Oz Terra (see Feature 9 in Figure 1B as an example). Unit ct_2 craters are characterized by their sizes $D <$ 35 km and their impact deposits, displaying rampart-like

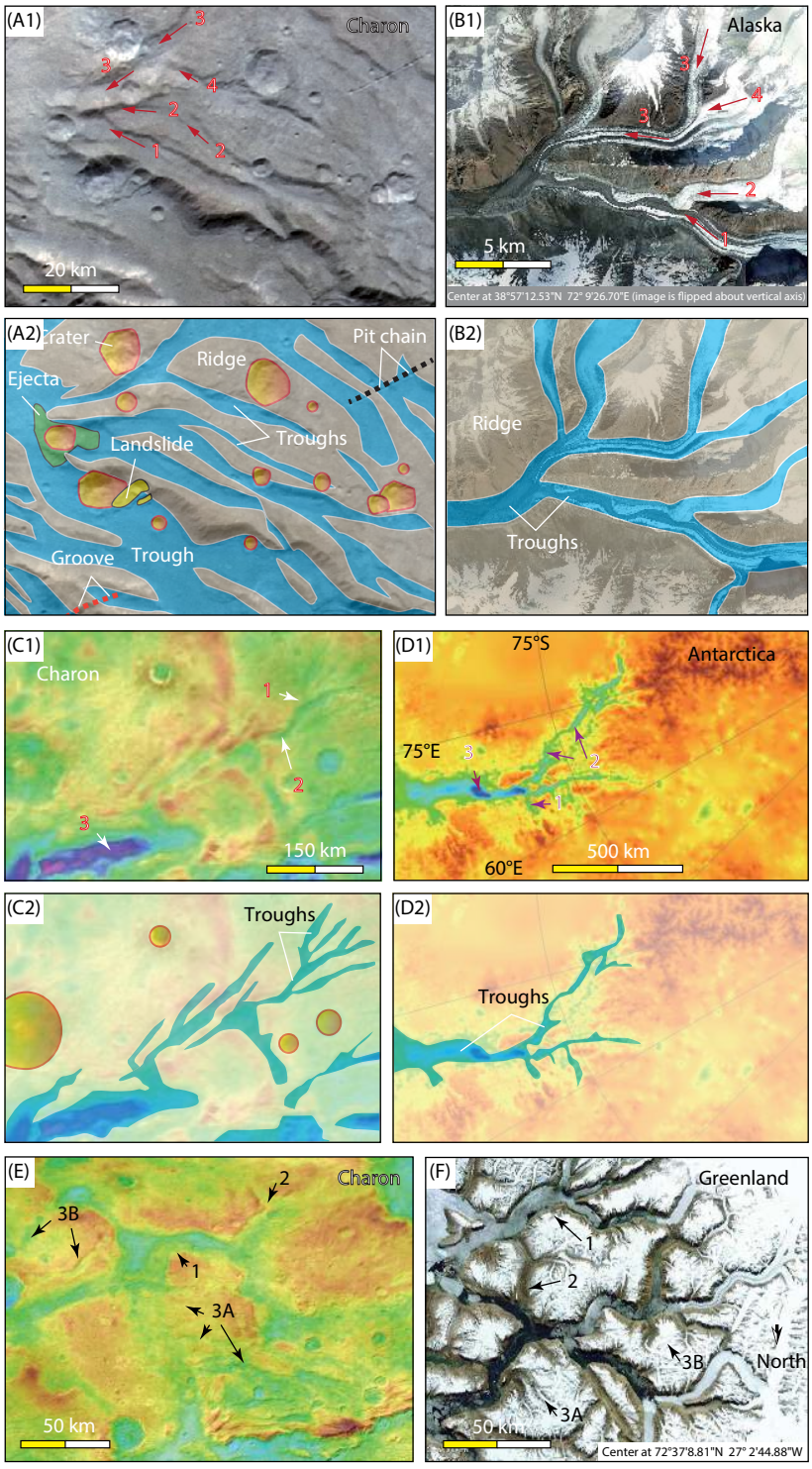

Figure 6. Comparison of Charon's dendritic and polygonal trough systems with possible analogues that have similar shapes and known origins from Earth. (A)–(B) Comparison of dendritic trough systems on Charon (image ID PIA 19967 in NASA's Photojournal Image Database) (A); and on Earth (B) from the Karakoram Mountains of central Asia taken from Google Earth™. Features 1 to 4 in both images are corresponding landforms with similar shapes. (C)–(D) Comparison of digital elevation models (DEMs) of a dendritic trough network on Charon (C) from Schenk et al. (2018a), and a subglacial dendritic network of troughs in Antarctica (D) with data from Fretwell et al. (2013). Note that both images display hanging-valleys (Feature 1), undulating longitudinal profiles (Feature 2), and overdeepenings along the main trough trunks (Feature 3). (E)–(F) Comparison of polygonal networks of wide (10 s·km) and long (100 s·km) troughs on Charon (E) with the digital elevation model from Schenk et al. (2018a), and on Earth (F) with the Google Earth™ image from a glaciated region of Greenland. Note the similarities in size and shape of the troughs (Feature 1), the presence of hanging valleys terminating at main trunks (Feature 2), and minor trough networks on the surface of trough-bounded plateaus (Features 3A and 3B).

morphologies as mentioned above (see Feature 10 in Figure 1B as an example) (also see Robbins et al., 2018). Although direct cross-cutting relationships between Unit ct_1 and Unit ct_2 are not observed, the consistently smaller sizes (< 35 km) of Unit ct_2 craters and their well-preserved ejecta deposits and rim ridges imply that Unit ct_2 have younger ages. Unit ct_3 is characterized by pristine crater morphology (see Feature 11 in Figure 1B as an example) and have their radial ejecta rays superposed over Unit ct_1 and Unit ct_2 craters. Note that craters of each type are selectively mapped in Figure 1C to avoid a clogged map presentation of other landform units.

5.2 Possible Analogues from Earth, Mars, Mercury, and Pluto

To assist the interpretation of our newly created geomorphological map (Figure 1C), we compare landforms on Charon systematically to solar-system analogues that have similar shapes and well-understood formation mechanisms. First, dendritic networks of troughs on Charon (Figures 6A and 6C) resemble glacial valleys (Figure 6B) or subglacial meltwater channels (Figure 6D) (Fretwell et al., 2013) on Earth. Note that the trough systems on both solar-system bodies display hanging valleys, steep-walled linear and curvilinear depressions, undulating longitudinal profiles, and overdeepenings (see detailed descriptions in the captions of Figures 6A–6D). On Earth, undulating longitudinal profiles are characteristic of subglacial meltwater channels (Grau Galofre et al., 2020), and overdeepenings are common along terminal troughs of subglacial meltwater-channel systems (Cook and Swift, 2012). Minor landslides mapped by Beddingfield et al. (2019) are also shown in Figure 6A. Landslides originated from steeply scarped range flanks in a rift-like valley on Charon resemble those in Valles Marineris (e.g., Lucchitta, 1979) on Mars, interpreted as a rift (e.g., Mège and Masson, 1996) or a transtensional left-slip fault zone (Yin A, 2012a): the Charon landslides are restricted to the base of the valley-bounding scarps (Beddingfield et al., 2019), whereas the Valles Marineris landslides may extend across most of and in some cases the entire floor of the graben-like valleys (cf., Lucchitta, 1979; Watkins et al., 2015, 2020).

Second, polygonal networks of troughs on Charon (Figure 6E) are similar in length scales, map patterns, trough-intersection angles, and trough depths to polygonal networks of glacial valleys in the Greenland region on Earth (Figure 6F). Note that the glaciated valleys on Earth are exposed in the foreland of the active Greenland sheet that was much larger and covered the entire land and shelf areas of Greenland during the last glacial maximum (Funder et al., 2011). Hence, the region shown in Figure 5F could have been generated initially below an ice sheet followed by valley glaciation.

Third, the troughed highland terrain (Unit *th* in Figure 1C) and the knobbed plains (Unit *sp*) along the northern margin of Vulcan Planitia (Figure 7A) resemble those on Mars created by rock glaciers (Figure 7B) (Kronberg et al., 2007). Both areas host partially filled craters, U-shaped valleys, and scattered knobs, rampart craters, and moated mounds on the foreland plains. In addition, both areas expose lobate aprons and knob trains (Figures 7C and 7D). The latter is interpreted to have been created by rock glaciers based on comparisons against analogues from the Earth (Kronberg et al., 2007). The most direct comparison of lobate aprons on Charon (Figure 7C) is to those exposed on Pluto (Figure 7E) that are interpreted to have been induced by N_2-ice glaciation with water-ice boulders as glacial tills forming the lateral and frontal moraines (Howard et al., 2017). Image resolution prevents more detailed comparison of landforms between Pluto and Charon at this time. However, the occurrence of lobate-shaped landforms on both bodies is undeniable; their close association with isolated knobs or knob trains is readily explained as glacial moraines, as discussed in Howard et al. (2017). This in turn implies that Charon may have experienced N_2 glaciation. Because the surface of Charon is composed of ammoniated water ice that is involatile (Protopapa et al., 2021), the inferred glaciers on Charon may have been composed of volatile N_2 ice that was removed during deglaciation (i.e., much like water ice on Earth) and involatile ammoniated H_2O ice (much like the rock debris on Earth) that stayed after deglaciation.

Fourth, the ridged plains on Charon (Figure8A) resemble piedmont moraine ridges on Earth (Figure 8B) (Sharp, 1958). In this comparison, the curvilinear round-topped ridges on Charon represent folds, whereas the isolated blocks mingled with the ridges may represent erratic boulders.

Fifth, ridge flanks with linear grooves and linear trains of smaller knobs on Charon (Feature 1 in Figure 8C) resemble a glacially striated surface on a ridge flank on Earth (Figure 8D) (Jakobsson et al., 2016). Parallel sets of evenly spaced linear grooves and ridges on glaciated surfaces are generally referred to as glacial flutes (Gordon et al., 1992; on Earth they are known as mega-scale glacial lineations when their length exceeds > 5–10 km (Clark, 1993). The linear grooves and linear knob chains on the ridge flank shown in Figure 8C are > 30–50 km in length, which on Earth would qualify them as mega-scale glacial lineations, created by fast-flowing ice streams, which are like rivers bounded by stagnant ice on their two sides (Clark, 1993; King et al., 2009). Mega-scale glacial lineations up to ~17 km in length hosted by a glaciated landscape have been documented in the Tharsis rise region of Mars (Yin A et al., 2021).

Sixth, lobate ridges on Charon (Figure 8E) resemble those created by rock glaciers on Earth (Elliott-Fisk, 1987) (Figure 8F). In this comparison, the convex direction of the lobate ridges would indicate the glacial flow direction, whereas boulders associated with the lobate ridges on Charon would represent glacial erratic deposits.

Seventh, moated mounds and rampart craters on Charon and Mars (Kronberg et al., 2007) are similar in shapes but differ by their topographic reliefs: the relief on Charon is ~3 km (Figures 9A and 9B) whereas the relief on Mars is only ~100 m (Figures 9C and 9D). The general similarities of the rampart craters on Charon and Mars were noted earlier (Kronberg et al., 2007); both display higher rim ridges and lower ejecta-terminus ridges, as shown in Figures 9E–9H. The origin of rampart craters on Mars has been attributed to the presence of ground ice or buried glaciers (Carr et al., 1977; Weiss and Head, 2013). For the moated mounds acting as rock debris flowing on top of a viscous glacial material, their elevations

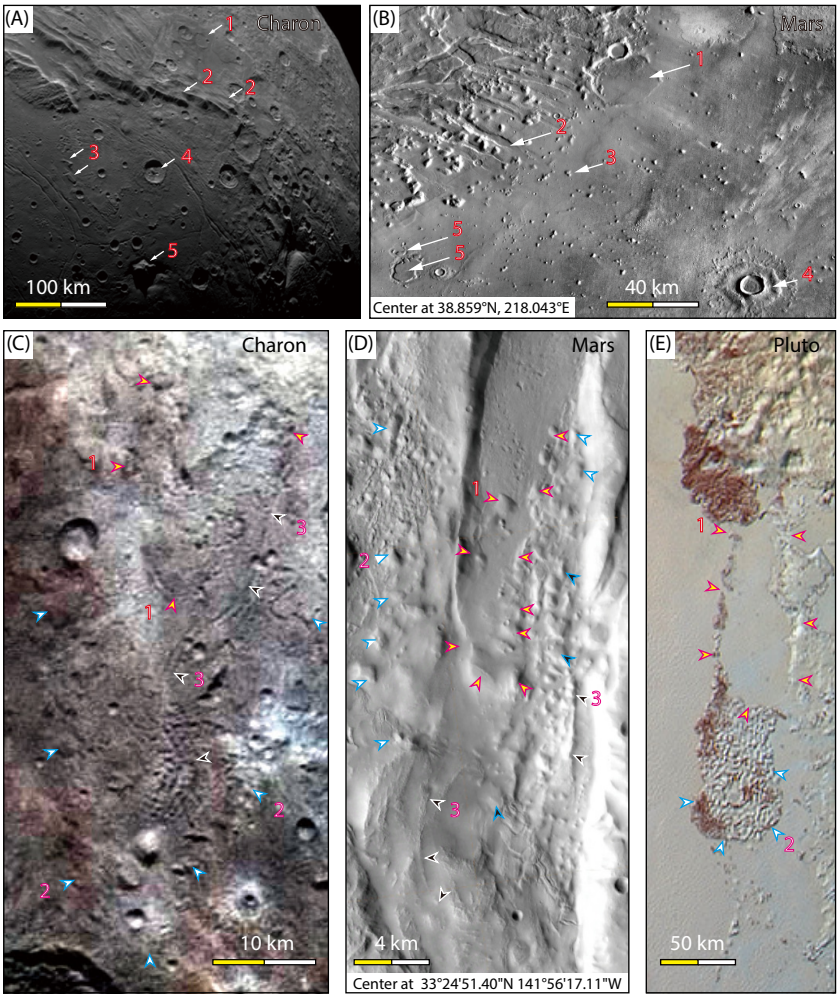

Figure 7. Comparison of Charon's landforms with possible analogues that have similar shapes and known origins from Mars and Pluto. (A)–(B) show comparison of troughed highlands and their knobbed foreland plains on Charon (A) (image ID mp1_0299180334_0x530_sci at a resolution of 622 m/pixel), and Mars (B) (THEMIS IR daytime image at a resolution of 100 m/pixel). Feature 1, a partially filled crater basin; Feature 2, steep-walled U-shaped valleys cutting across the highlands; Feature 3, scattered knobs in the foreland plains; Feature 4, rampart crater; and Feature 5, moated mounds. (C)–(E) are images from Charon (C) (image ID PIA 19967 in NASA's Photojournal Image Database), Mars (D) (THEMIS IR daytime image at a resolution of 100 m/pixel), and Pluto (E) (image cropped from the Pluto Global Mosaic (Schenk et al., 2018b)) that show similar lobate features and distributed knob trains that define the rim of the lobes.

above the flat surrounding surface should have been controlled by isostasy: higher mounds with deeper roots and lower mounds with shorter roots.

Finally, deformation-modified craters on Charon are best expressed by crater-rim offset, removal, and truncation, which are closely associated with linear or curvilinear north-trending scarps that bound the north-trending ranges (Figures 10A and 10C). The crater-offset scarps in Figure 10A and those shown in Figure 3B (see detailed description in its caption) resemble the thrust-induced scarps on Mercury (Figure 10B) (Watters et al., 2015). The truncated craters on Charon as shown in Figures 10A and 10C resemble the crater-truncated Thaumasia thrust (Figure 10D) bounding the eastern edge of the Tharsis rise on Mars (Nahm and Schultz, 2010; Yin A, 2012b).

5.3 A Landscape Evolution Model of Charon

To account for the major observations listed above, we take a system approach. Specifically, our system-based landscape model must explain the spatiotemporal relationships of all landform units and major landform Features established by the early studies (Moore et al., 2016; Desch and Neveu, 2017; Robbins et al., 2017, 2018, 2019; Beyer et al., 2019) and this study (Figure 1). We propose a self-consistent tectono-geomorphological model for the geological evolution of Charon's encounter hemisphere (Figure 11). The model shown in Figure 11 is inspired by the well-established glacial landsystem-evolution models for Earth (e.g., Brodzikowski and Van Loon, 1987) that predict many landforms with shapes similar to those on Charon that we have mapped. The key ingredients of the model include (1) early formation of the impact-induced east-trending extensional belt along the northern margin of Vulcan Planitia, (2) younger north-trending thrusting due to Charon's despinning, (3) coeval thrusting and glaciation in the highland region (Oz Terra), and (4) glacial transport of water-ice debris into the Vulcan Planitia impact basin. The main evidence for past glaciation on Charon come from shapes similar

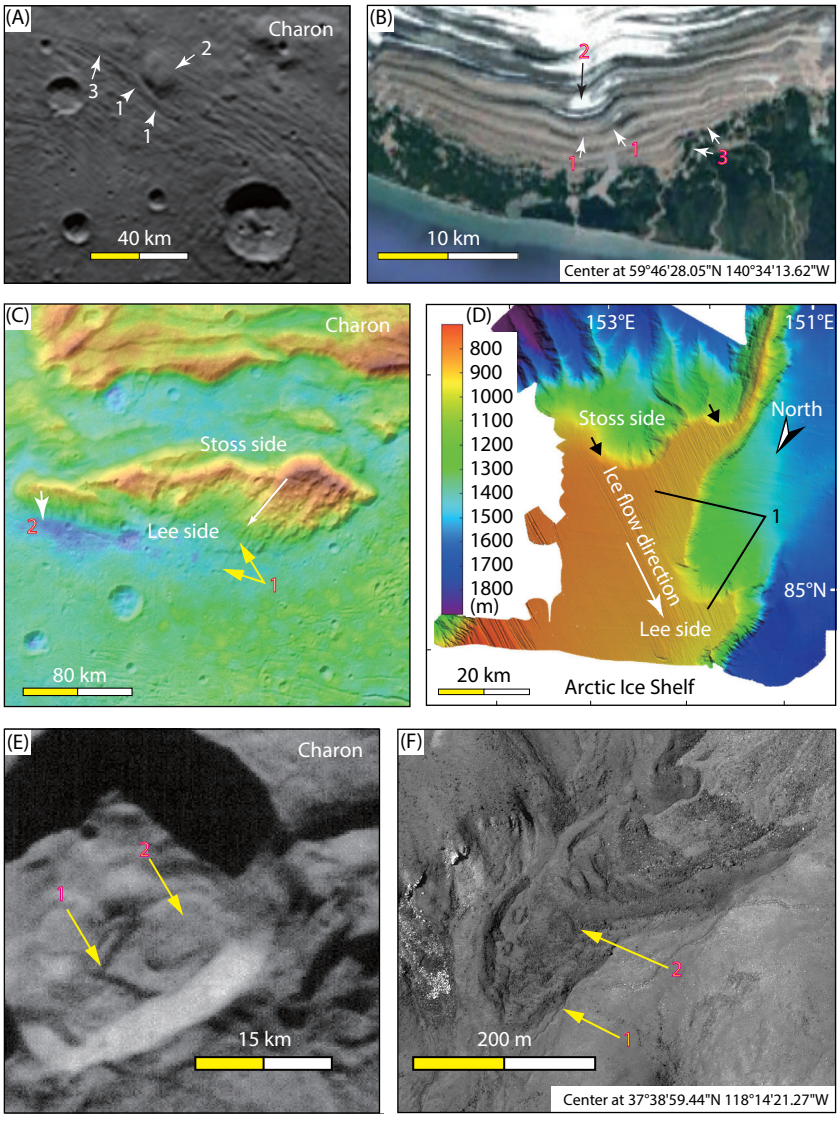

Figure 8. Comparison of Charon's landforms with possible analogues that have similar shapes and known origins from Earth. (A)–(B) Comparison of ridged plains on Charon (A) (image ID mp1_0299180334_0x530_sci at a resolution of 622 m/pixel), and ridged plains in the foreland region of the Malaspina Glacier in Alaska on Earth (B) with the image cropped from Google Earth™. The parallel ridges in front of the Malaspina glacier were formed by folding of debris-bearing glaciers (Sharp, 1958). Note the similarities in the shape of the curved ridges (Feature 1) that are deflected around local topographic heights (Feature 2) and the lateral merging of the ridges (Feature 3). (C)–(D) Comparison of digital elevation models of striated quasi-planar ridge flanks on Charon (C) (Schenk et al., 2018a) and on Earth (D) from an Arctic ice shelf adopted from Jakobsson et al. (2016). (E)–(F) Comparison of lobate ridges on Charon that fill a crater floor and lobate ridges composed of rock glaciers that fill a glaciated valley in the White Mountains of California (image cropped from Google Earth™).

to landforms on Earth, Mars, and Pluto that have known glacial/ground-ice origins (Figures 7 and 9). The support for east–west compression that created the north-trending, eastward convex, arcuate ranges comes from comparison with truncated and obliterated impact craters, modified by thrusting, on Mercury and Mars (Figures 10A–10D).

In our model, we envision that Charon experienced an initial phase of intense bombardments, expressed by the occurrence of the largest impact craters (D > 50–100 km) exposed on the encountered hemisphere. Following the early suggestion of Malamud et al. (2017), we agree that a giant impact created a Vulcan Planitia that was much deeper than its present depth (Figure 11A). We interpret the ridge-valley zone (Unit *rv* in Figure 1C) along the northern rim of the putative impact basin as an extensional fault zone created by the giant impact (Figure 11B). Note that Malamud et al. (2017) considered the east-trending extensional belt to have been created by global contraction followed by extensional reactivation, which is different from the scenario proposed here. An interesting consequence of the giant impact hypothesis is its injection of heat into Charon; the elevated temperatures would have favored not only cryovolcanism, as suggested by Malamud et al. (2017), but also the formation of a transient N_2-dominated atmosphere capable of driving N_2 glaciation.

A major issue with the giant impact hypothesis of Malamud et al. (2017) is the lack of impact ejecta deposits in Oz Terra (Beyer et al., 2019). In our model, we suggest that N_2-ice glaciation in Oz Terra,

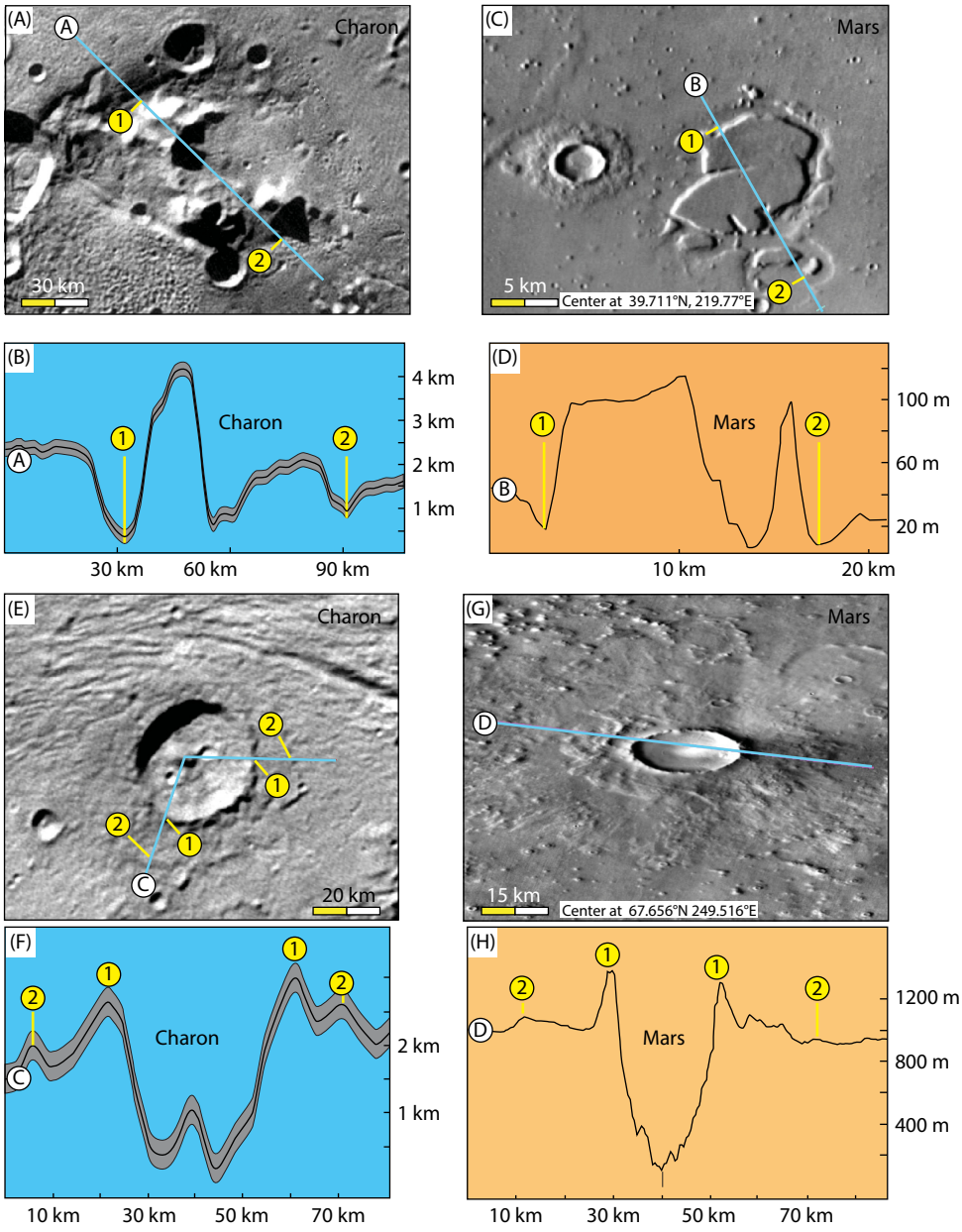

Figure 9. Comparison of moated mounds and rampart craters on Charon and Mars. (A)–(B) An image of a moated mound complex on Charon cropped from the Charon New Horizons LORRI MVIC Global Mosaic 300 m v1 (Schenk et al., 2018a) (A), and a topographic profile (B) obtained from the Charon digital elevation model created by Schenk et al. (2018a). Features 1 and 2 indicate the positions of the moat. (C)–(D) An image of moated mound complex on Mars (THEMIS IR daytime image at a resolution of 100 m/pixel) (C), and a topographic profile (D) constructed using the blended High Resolution Stereo Camera (HRSC) data and Mars Orbiter Laser Altimeter (MOLA) digital elevation model (DEM) at a resolution of 200 m/pixel (Fergason et al., 2018). Features 1 and 2 indicate the positions of the moat. (E)–(F) An image of a rampart crater on Charon cropped from the Charon New Horizons LORRI MVIC Global Mosaic 300 m v1 (Schenk et al., 2018a) (E), and a topographic profile (F) obtained from the Charon digital elevation model created by Schenk et al. (2018a). Feature 1 indicates the rim ridge and Feature 2 indicates the ejecta-terminus ridge. (G)–(H) An image of rampart crater on Mars (THEMIS IR daytime image at a resolution of 100 m/pixel) (G), and a topographic profile (H) constructed using the blended High Resolution Stereo Camera (HRSC) data and Mars Orbiter Laser Altimeter (MOLA) digital elevation model (DEM) at a resolution of 200 m/pixel (Fergason et al., 2018). Feature 1 indicates the rim ridge and Feature 2 indicates the ejecta-terminus ridge.

occurring after the giant impact, removed the impact-breccia deposits and transported them to the Vulcan Planitia basin. The same glacial-erosion process would be responsible also for the complete removal of impact ejecta deposits around the largest craters in Oz Terra, and partial or complete removal of their crater rim ridges.

The infilling of Vulcan Planitia by cryovolcanism could have occurred as envisioned by Beyer et al. (2019) prior to or during our proposed glaciation. However, cryovolcanism must have terminated prior to the final emplacement of water-ice-debris-bearing N_2 glaciers, which are expressed as parallel round-topped ridges mingled with blocks of various sizes—up to 10–20 km—and

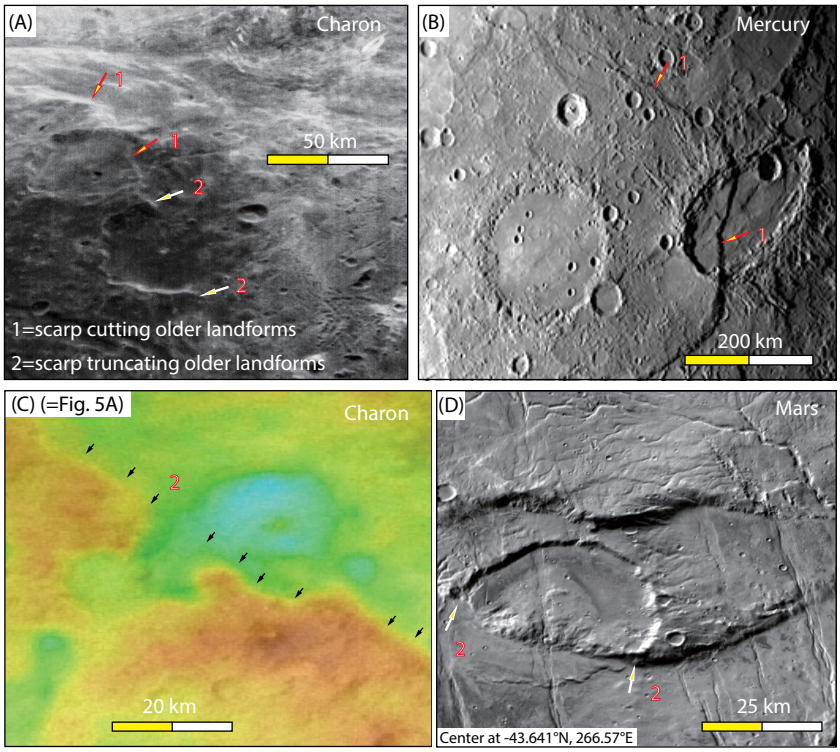

Figure 10. Comparison of deformation-modified craters on Charon, Mercury, and Mars. (A)–(D) Comparison of crater rim ridges either cut or truncated by scarps among those exposed on Charon, Mercury, and Mars. The Charon image in (A) is cropped from image lor_0299180409_0x630_sci_3 at a resolution of 154 m/pixel, the Mercury image showing Beagle Rupes in (B) is from PIA10939 in the NASA's photojournal database, and the Mars image in (D) is cropped from the CTX global mosaic displayed in JMARS. For (C), see Figure 5A.

shapes (Figure 11B). The ridges are interpreted as water-ice moraine landforms, and the blocks as water-ice erratic boulders (Figure 11B).

Supported by the similar patterns of trough networks on Charon and in a glaciated landform on Earth (Figures 6E and 6F), we suggest that glacial erosion was responsible for creating the orthogonal network of the first-order troughs in Oz Terra (Figure 11C). These channels could have been developed either below an ice sheet, or as glacial transport U-shaped valleys (as on Earth, shown in Figure 6F).

Similar morphologies for the truncated and obliterated craters on Charon, Mercury, and Mars (Figures 10A–10D) led us to suggest that the north-trending arcuate ranges were created by thrusting during east–west compression. In this interpretation, the eastward convex-shaped ranges should have been created by west-dipping thrusts. We suggest that the apparent offset of the north-trending ranges (Features 1 and 2 in Figure 1B) on the two sides of the valley zone (Unit *rv* in Figure 1C) was a result of crack arresting (Cooke and Underwood, 2001); that is, the older and weaker faults along the eastern extensional belt were reused as strike-slip transfer structures linking north-trending thrusts on its two sides (Figures 11D and 11E). The lack of rift shoulders along the western segment of the valley zone (i.e., Unit *rv* in Figure 1C) can be explained by syn- and post-thrusting glacial erosion (Figures 11D–11E).

Post-thrusting glaciation is expressed not only by the removal of rift-shoulder ridges but also by the development of younger dendritic networks of troughs (i.e., Unit tr_2 in Figure 1C) (Figure 11E). Possible Earth analogues (Figures 6B and 6D) imply that the dendritic troughs on Charon could have been formed either by valley glaciers or subglacial melt-channel development. The valley-glacier interpretation implies cold-based glaciation (i.e., the basal ice is frozen, the underlying bedrock and glacial movement being accommodated by ice creeping within the glaciers), while subglacial meltwater-channel interpretation implies at least local warm-based glaciation (i.e., melting that occurs at the base of an ice sheet). Under the cold-based condition, the pre-glacial landforms could be preserved as glacial flows that are accommodated primarily by ice-sheet deformation without the involvement of subglacial tills and subglacial bedrock (e.g., Waller, 2001). In contrast, wet-based glaciation should have created streamlined landforms (e.g., Evans et al., 2006), which are absent next to the interpreted dendritic channels. This led us to suggest that the dendritic channels may have been developed as glacial valleys, not meltwater conduits. This interpretation is consistent with the presence of hanging valleys in the dendritic channel systems (e.g., Figure 3C). Some dendritic channels on Charon are associated with pyramids, arêtes, U-shaped valleys, and hanging valleys (see Figures 5E and 5F), which are best explained by their formation of valley glaciation.

Based on analogues from Mars (Kronberg et al., 2007) (Figures 7B–7D and 9C), we speculate that Vulcan Planitia may have been filled by rock glaciers; that is, water ice as the bedrock debris that covers N_2 ice below (Figure 11E). In this interpretation, the polygonal-shaped blocks/mounds/mountains of various sizes (up to

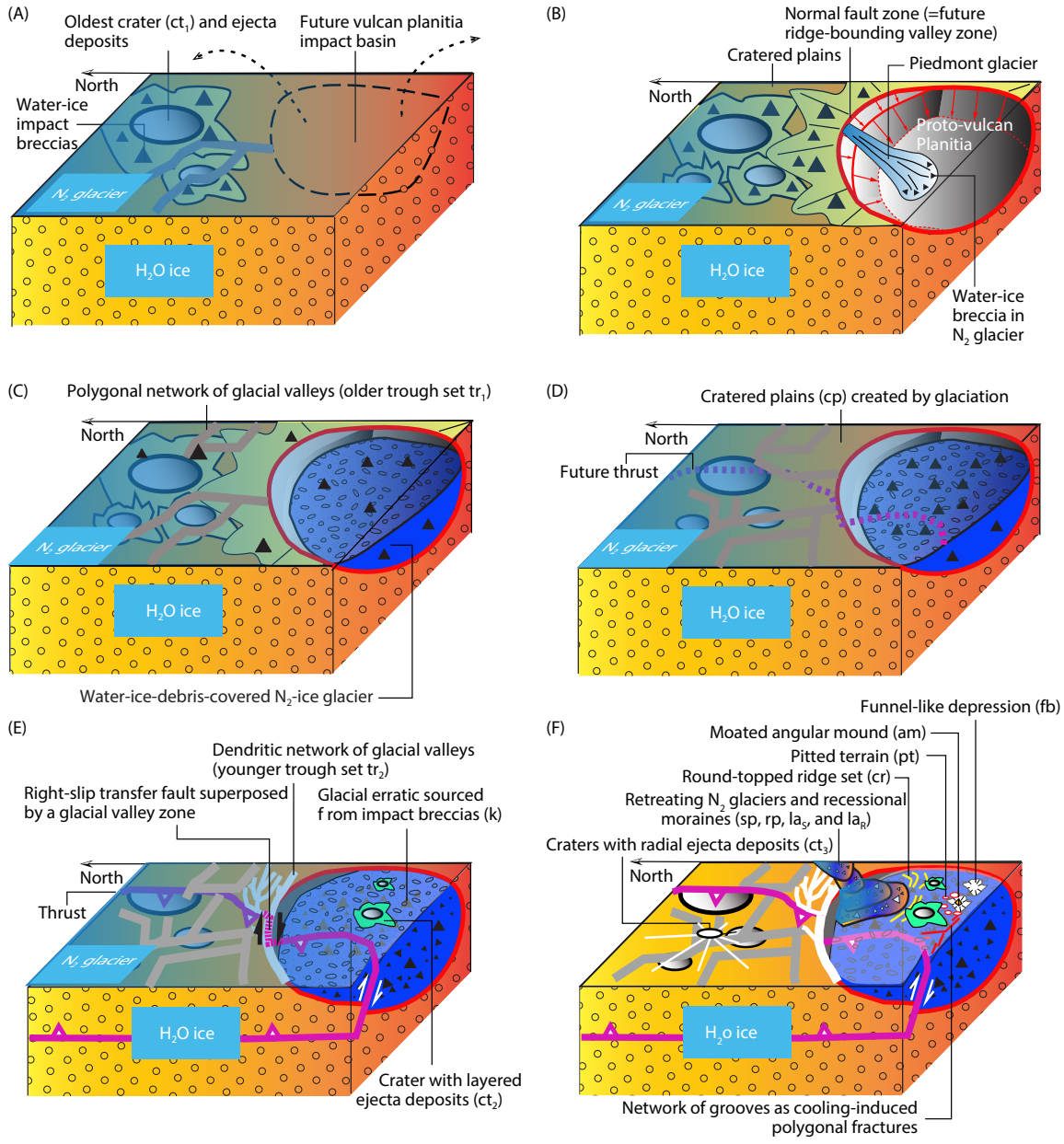

Figure 11. Landscape evolution of Charon's encounter hemisphere. (A) Intensely bombarded surface of Charon immediately after its formation was characterized by larger craters (D > 50 km) with water-ice breccia-bearing ejecta blankets. Although not shown, glaciation could have been coeval during the early intense bombardment. (B) The early intense bombardment by impacts immediately after the formation of Charon was responsible for formation of proto-Vulcan Planitia, which was deeper than its present depth and surrounded by impact-induced normal faults and fault-bounded grabens. Again, glaciation could have occurred during the formation of proto-Vulcan Planitia. (C)–(D) Glaciation on the highlands of Oz Terra removed the older impact breccias, eroded the older crater-rim ridges, and infilled the older crater basins. Meanwhile, heating from below and basal pressure due to the weight of the N_2 ice sheet above caused development of subglacial N_2-liquid channels. Removed impact breccias from Oz Terra were transported by N_2 glaciers to Vulcan Planitia. The progressive accumulation of water-ice blocks, and their potentially smaller densities than the viscous N_2 ice, created a situation that glaciers in Vulcan Planitia were now mostly covered by water-ice debris that protected N_2 ice from being sublimated. (E) Syn-glaciation thrusting created north-trending arcuate ranges. The same thrusting event also affected the western margin of Vulcan Planitia. The lateral propagating north-trending thrusts were arrested by the pre-existing weak east-trending normal fault zone, which was induced by a giant impact mentioned above and marks the topographic boundary between Oz Terra and Vulcan Planitia. Impacts in Vulcan Planitia created craters surrounded by layered ejecta blankets with steep terminations. These craters are similar to rampart craters on Mars interpreted to have been generated in regions with subsurface ground-ice layers (Watters et al., 2015). (F) Deglaciation created recessive moraine landforms and deposits. Cooling of the water-ice-debris-covered N_2 ice created polygonal networks of fractures, while sublimation of the N_2 ice created pitted terrains. Finally, continued cooling led to an increase in the viscosity of the debris-covered N_2 glaciers. The increasing glacier viscosity eventually terminated the sinking process of the mega-erratic boulders in Vulcan Planitia. Meanwhile, the high-viscosity, debris-covered glaciers prevented viscous relaxation of the moats around the mega-erratic boulders, which is expressed as polygonal funnel-like depressions.

> 30 km across) with or without moated margins are interpreted as floating water-ice blocks. Their various elevations are controlled by isostasy: higher-elevation blocks, mounds, and mountains in Vulcan Planitia should have deeper roots extending into the low-viscous nitrogen ice below.

We suggest that the formation of recessional moraines resulted in the development of lobate ridges, lobate aprons, knob trains, and isolated knobs composed of water ice. The isolated knobs in Oz Terra are interpreted as to be the same as the blocks in Vulcan Planitia, which represent erratic boulders composed of water ice and originated from impact breccia (Figure 11F).

It is likely that deglaciation was associated with rapid sublimation and eventual removal of N_2 ice under a thinner atmosphere. The cooling due to atmospheric thinning may have created tensile fractures across Vulcan Planitia, resulting from unstable extension of a rheologically stratified system (Fletcher and Hallet, 1983; Yin A, 2000); in this case, the brittle water-ice debris layer overlies the viscous N_2-ice layer. The rapid cooling event may have also frozen mega-breccia of water ice on the way to sinking into the subsurface viscous N_2-ice layer below Vulcan Planitia. The rapid freezing is expressed as moated margins around the polygonal mounds/mountains and the formation of funnel-like depressions (Figure 1C).

The thickness of glaciers across Oz Terra is estimated to be ~2–3 km, constrained by the topographic relief of the first-order orthogonal troughs interpreted as glacial valleys (i.e., Unit tr_1 in Figure 1C; also see Figures 2A–2D). In contrast, the thickness of the glaciers across the east-trending valley zone (Unit *rv* in Figure 1C) along the boundary between Oz Terra and Vulcan Planitia is estimated to be > ~5 km, constrained by the elevation difference between the striated ridge flank that we interpret as the site of ice-stream flow, and its bounding valley floors that we interpret as regions of stagnant ice (see Figure 8C and related interpretations).

5.4 Plausibility of Our Proposed Glaciation Model

The similarity of landforms on Charon (this study) and Pluto (Howard et al., 2017) to those created by glaciation on Earth raise the question of why these solar-system bodies with drastically different gravities, surface compositions, and atmospheres would have operated in such a way. As argued by Collins et al. (2010), the similar homologous temperature (T_H) of rocks on Earth and water ice in the outer solar system may have played a first-order role in generating similar styles and shapes of tectonic structures on Earth and icy satellites. The homologous temperature of a material is defined by the ratio of the averaged deformation temperature (T_D) to its melting temperature (T_M) (Goetze, 1978; Weertman, 1983). Below, we compare the homologous temperatures of glaciers and bedrock on Earth and Charon.

In the polar regions of the Earth, T_H for H_2O ice is ~0.81 assuming T_D = 223 K and T_M = 273 K, and T_H for felsic rocks is ~0.24 assuming T_D = 223 K and T_M = 923 K. In comparison, glaciers on Charon are likely to have been composed of N_2 ice (although they have been sublimated away by now), similar to the interpreted N_2-ice glaciers carrying water-ice debris on Pluto (Howard et al., 2017). The bedrock of Charon is composed of ammoniated water ice ($NH_3{\cdot}nH_2O$) (Protopapa et al., 2021) that has T_D = ~50 K, T_M (N_2) = ~63 K, and T_M ($NH_3{\cdot}nH_2O$) = ~176 K, respectively; these values yield T_H for N_2 ice on Charon to be ~0.79 (cf. 0.81 for water ice on Earth) and T_H for $NH_3{\cdot}nH_2O$ ice on Charon to be ~0.28 (cf. 0.24 for felsic rocks on Earth). The above comparison indicates that the homologous temperatures of glaciers and bedrocks on Earth and Charon are nearly identical.

In order to explain the ~30 : 1 ratio for the maximum heights of the moated mounds on Charon (~3 km) and Mars (~100 m), we assume that the inferred bedrock debris on top of viscous glaciers must have had plastic strengths of Y_C and Y_M for Charon and Mars, respectively. Equating the plastic strength to the vertical load requires $Y_C = \rho_C g_C h_C$ and $Y_M = \rho_M g_M h_M$, where ρ_C = 1000 kg·m^{-3} is the water ice density, ρ_M = 2300 kg·m^{-3} is rock debris density, and g_C and g_M are the surface gravity of Charon (0.288 m·s^{-2}) and Mars (3.72 m·s^{-2}). Because brittle materials such as rocks and water ice have similar mechanical strengths (Byerlee, 1978; Schulson, 2001), $Y_C/Y_M \approx 1$ would require $h_C/h_M \approx 29.7$ using the physical quantities mentioned above. This estimated h_C/h_M ratio is very similar to the observed ratio of ~30 : 1. The above analysis implies that the debris-cover layer is a viscoplastic material: a block sinks if its weight-induced pressure is larger than the plastic yield strength of the layer but stays on top if its weight-induced pressure is smaller than the yield strength. Note that the elevation of the blocks, once sunk into the subsurface viscous layer of nitrogen ice, are controlled by isostasy.

5.5 Predictions of the Proposed Landscape Model

Our proposed landscape-evolution model (Figure 11) provides new insights into some of the interesting observations made by previous researchers. The lower-than-expected number of $D \lesssim$ 10–20 km craters in Vulcan Planitia (Singer et al., 2019) can be accounted for by a combination of glacial erosion, glacial deposition, and glacier flow, possibly superposed on an earlier fluvial landscape. This means that the size-frequency distribution (SFD) of craters on Charon should be regarded only as a lower bound when used to test competing models of planet formation during the evolution of the Solar System (e.g., Schlichting and Sari, 2011). Additionally, the landscape model in Figure 11 provides an alternative explanation of why craters on Charon are consistently shallower than those of Saturn's icy moons with similar surface gravity and ice compositions (Schenk et al., 2018a). Schenk et al. (2018a) suggest that the shallower crater depths on Charon may have been induced by slower impact velocities in the Kuiper belt. In our model, we suggest that the observed shallower depths can be demonstrated as a combined result of rim-ridge erosion and crater-basin infilling.

As shown by Malamud et al. (2017), amorphous water ice in their cold-start model should have been un-processed by heating throughout the evolution of Charon. If Charon evolved in such a way, its surface exposure of crystalline water ice exclusively along the north-trending ranges in Oz Terra requires an explanation (Protopapa et al., 2021). In our model, the exposure of the crystalline ice in these mountain ranges is explained by thrusting and glacial erosion. That is, deeper crystallized water ice, formed at hotter temperatures, was brought up to the surface by thrusting.

The alternative hot-start models (e.g., Beyer et al., 2019) would predict global exposure of crystalline water ice. But such a model does not explicitly explain where and why the highest volumes and largest grain sizes of crystalline water ice are exposed only along the north-trending ranges in the encounter hemisphere of Charon (Protopapa et al., 2021).

Our proposed north-trending thrusting, as the cause of arcuate-range formation in the equatorial and low latitude regions, is compatible with a stress field generated by despinning of Charon during its receding course from—but before being tidally locked on a circular orbit around—Pluto (Matsuyama and Nimmo, 2013; Barr and Collins, 2015; Rhoden et al., 2020). However, despinning alone does not explain why the range-bounding thrusts dip consistently to the west, as required by the eastward convex shape of the arcuate ranges. On Earth, thrusts with the same dip direction are commonly parts of a structural system bounded below by a unidirectionally moving basal decollement (e.g., Boyer and Elliott, 1982). Based on this insight, we interpret the west-dipping thrusts on Charon to be parts of an east-directed thrust system (Figure 12). We suggest that the mechanically favored location for the inferred decollement may lie along the brittle-ductile transition zone, and that the top-east flow in the ductile ice may have been driven by warm-ice convection. This speculation could be modelled to a greater degree in future studies.

The timing and duration of our proposed glaciation are unconstrained. Based on the current dating, using crater size-frequency distributions (Singer et al., 2019), our mapped glaciated terrains should have ages of > 4.0 Ga. This means that the maximum duration of glaciation could be as long as ~500 Ma. Such protracted glaciation is possible considering the recent work on Pluto's atmosphere that shows its escape rate to be four orders of magnitude slower than the theoretical expectation (Gladstone et al., 2016), possibly due to the presence of dust in Pluto's atmosphere (Zhang X et al., 2017; Lavvas et al., 2021). Glaciation on Charon could have occurred as a single event, or as multiple events. The latter may have been induced by Charon's complex climate history (Hansen and Paige, 1996; Bertrand et al., 2018; Johnson et al., 2021) or by comet impact events (Stern et al., 2015).

Our proposed landscape-evolution model makes the following testable predictions. First, the knobs scattered in Vulcan Planitia should have different volume contents and grain sizes of crystalline water ice, reflecting their different origins at various depths of the ice shell in Oz Terra, excavated to the surface by impacts and transported to the lowland plains by glaciation. This prediction can be tested by using spatially resolved IR spectra acquired with the Linear Etalon Imaging Spectral Array (LEISA), which is part of the New Horizons Ralph instrument (Reuter et al., 2008). Because the best LEISA scan of Charon is at a spatial resolution of ~5 km/pixel (Protopapa et al., 2021), only the largest knobs can be differentiated by this data set. Second, Vulcan Planitia should contain debris-covered glaciers. This prediction can be tested using orbitally based ground-penetrating radar techniques such as have been used to identify rock glaciers on Mars (Holt et al., 2008). Third, the inferred thrusts should have generated foreland-basin deposits, and their internal beds should thus be thickening towards the interpreted thrust traces; and the beds next to the thrusts should be folded. Similarly, the western segment of the valley zone, interpreted to have an extensional origin, should have preserved rift-basin deposits even though the valley-bounding rift shoulders have eroded away. The rift-basin deposits should show tilted strata dipping opposite to the dip of the nearby basin-bounding fault. The above predictions between faults and syn-faulting sedimentation can be tested using orbitally based ground-penetrating radar techniques (Phillips et al., 2008). Fourth, Vulcan Planitia as a giant impact basin can be tested when complete imaging of Charon is achieved.

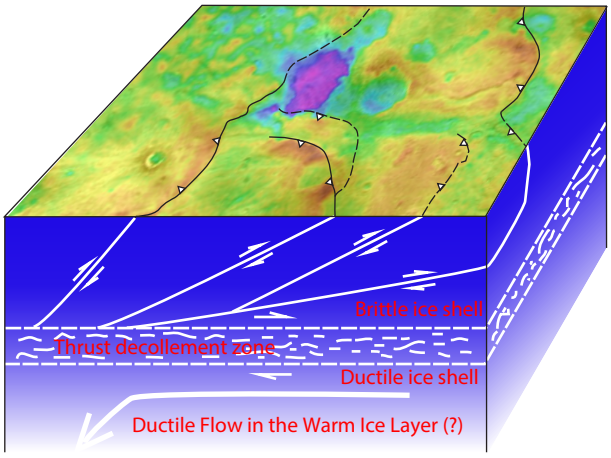

Figure 12. A block diagram showing the relationship between the interpreted west-dipping thrusts and a possible top-to-the-east thrust decollement zone in the brittle-ductile transition zone of Charon's ice shell. Solid lines are thrust traces expressed as curvilinear scarps or range fronts that either truncate or offset older craters. The dashed lines are inferred thrust traces lacking fault-scarp-like morphologies. Triangles indicate hanging-wall sides of thrusts.

5.6 Implications for the Evolution of Larger KBOs

An implication of our work is that larger KBOs with sizes equal to or greater than Charon may have evolved from an initial stage (Figures 13A and 13D) characterized by the presence of a N_2-dominated atmosphere capable of driving N_2-liquid activities. A possible analogue for this stage of evolution is Titan but with an important difference: the fluvial agent on Charon is nitrogen whereas the fluvial agents on Titan are methane and ethane (Stofan et al., 2007; Lorenz et al., 2008; Hayes et al., 2018). The gravity and atmospheric pressure conditions may also differ between these two solar-system bodies. Here, we simply emphasize the possible surface processes on larger KBOs during this initial stage. Although there is no direct evidence for fluvial activities on Charon, it is possible that the interpreted dendritic glacial-valley networks originated from fluvial channels. The duration of this stage is unconstrained, but it most likely occurred in the first few million years after the Charon-forming impact with its temperature enhancement of ~30 K (McKinnon et al., 2021) or immediately after the giant impact that created the Vulcan Planitia basin.

During the second stage (Figures 13B and 13D), Jeans escape and hydrodynamic escape (Hunten, 1982; Brain et al., 2016) in conjunction with impact erosion may have caused the gradual

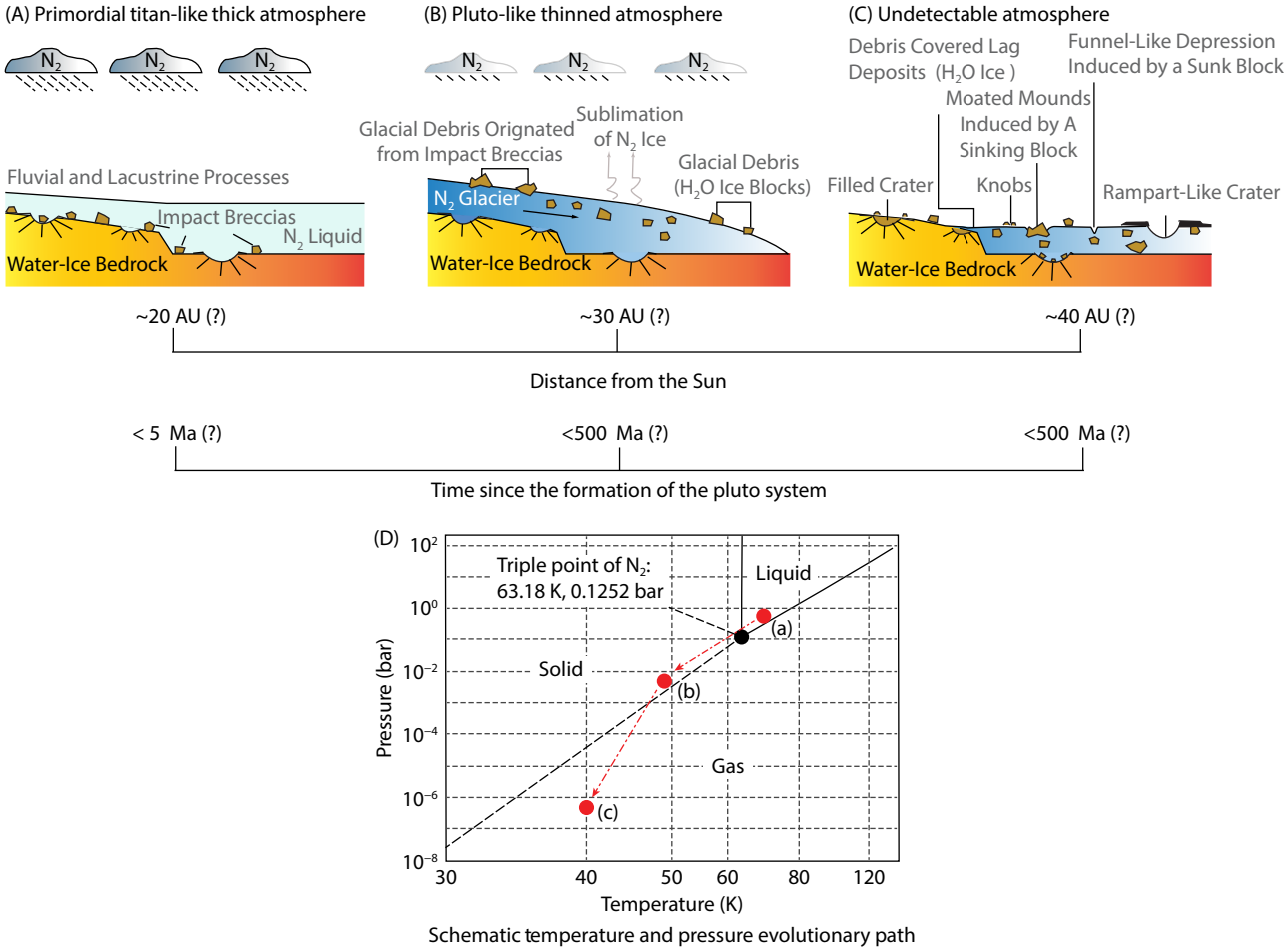

Figure 13. A hypothetical evolutionary path of larger Kuiper belt objects. (A) A warm start; a thick atmosphere supports liquid N_2 activities. (B) Atmosphere thins progressively, cooling the surface, leading to glaciation. (C) Atmospheric loss causes rapid sublimation of N_2 ice, which in turn causes rapid cooling, creating a frozen landscape that retains a snapshot of the on-going geologic process at the time of the rapid cooling event. (D) Schematic temperature–pressure evolutionary path on the nitrogen phase diagram, modified from Fray and Schmitt (2009).

thinning of the primordial atmosphere of the larger KBO. Meanwhile, termination of gravitational accretion and waning impact bombardments reduced surface heating. The combined effect of atmospheric thinning and reduction of heat release have led to surface cooling, which allowed the transition from a landscape shaped mainly by fluvial processes to a landscape shaped mainly by glaciation. Pluto, with a thin atmosphere and ongoing glaciation, may serve as a modern analogue for this stage (Figure 13B) whose duration may be as long as 500 Ma, as exemplified by Charon.

In the final stage, the primordial atmosphere was completely removed and the internal heat sources were largely exhausted. The resulting low surface pressure caused rapid sublimation of N_2-ice glaciers, which in turn caused rapid cooling and runaway N2-ice removal. This process must have occurred rapidly so that viscous-deformation processes expressed by moated mounds and funnel-like depressions were frozen into the modern landscape (Figures 13C and 13D). Current Charon, without a detectable atmosphere, may serve as an example of this stage.

The time scale for the rapid cooling phase that led to the creation of the moated mountains and funnel-like depressions should be less than ~1000 years based on a simple calculation below. We assume that the moated mounds in Vulcan Planitia are sinking rigid blocks and that their average density is ~1 kg/m^3 greater than the underlying N_2 ice. For a spherical mound with a diameter of ~20 km, the downward velocity of the mound according to the Stokes law would be ~10^{-10} m/s given the N_2-ice viscosity of ~10^{14} Pa·s. Using the moat depth of 1–2 km (Figure 9) as a constraint for the magnitude of the downward motion, the time scale required for the sinking mound is between 300 and 600 years. Note that the above estimates depend critically on the viscosity of N_2 ice. The lack of information on the strain rate during the inferred sinking of the moated mounds, a critical factor in determining the effective viscosity of N_2 ice (Yamashita et al., 2010), prevents us from exploring this issue any further.

6. Conclusions

A systematic geomorphological mapping and detailed landform analysis using the highest resolution images obtained by the New Horizons spacecraft reveal the presence of a range of differentiable terrains that were not examined in detailed by the early studies. These terrains and their cross-cutting relationships define a complex spatiotemporal evolution of the ice shell and the surface

morphology of Charon's encountered hemisphere. The most important findings of our work include:

(1) truncation and presumed obliteration of large craters (diameters > 30–40 km) and their crater rim ridges along the eastern edges of several north-trending, eastward-convex, arcuate ranges in Oz Terra of the northern encountered hemisphere;
(2) lobate ridges, lobate knob trains, and lobate aprons resembling glacial moraine landforms on Earth;
(3) dendritic channel systems containing hanging valleys; and
(4) locally striated surfaces defined by parallel ridges, knob trains, and grooves that are > 40–50 km in length.

The above observations and the topographic dichotomy of Charon's encountered hemisphere can be explained by a landscape-evolution model that involves (i) a giant impact that created the Vulcan Planitia basin and the extensional fault zone along its northern rim, (ii) a transient atmosphere capable of driving N_2-ice glaciation, eroding the water-ice bedrock and transporting water-ice debris to sedimentary basins, (iii) regional glacial erosion and transport of earlier emplaced impact eject deposits from the highlands of Oz Terra into the lowland basin of Vulcan Planitia, (iv) syn-glaciation north-trending thrusting, interpreted to have been induced by Charon's despinning, and (v) the development of a water-ice debris cover layer over subsurface N_2 ice below Vulcan Planitia during global deglaciation. The infilling of the Vulcan Planitia could have been accompanied by cryovolcanism. The extensive modification of impact craters means that the crater size-frequency distributions from Charon should serve only as a lower bound when used to test the formation mechanism of Kuiper belt objects.

Acknowledgments

This research would never have been possible without the dedicated effort of the New Horizons Team, whose persistence and intellectual leadership led to exciting discoveries of a remote world that was previously all but unknown to humans. We thank the New Horizons Team especially for making their data not only available to the public but in a format that outsiders can use directly for meaningful research. This study is a result of curiosity-driven research not funded by any agencies. Our work benefited greatly from discussions with our colleagues Dave Paige and Hilke Schlichting at UCLA.

References

Abod, C. P., Simon, J. B., Li, R. X., Armitage, P. J., Youdin, A. N., and Kretke, K. A. (2019). The mass and size distribution of planetesimals formed by the streaming instability. II. The effect of the radial gas pressure gradient. *Astrophys. J.*, *883*(2), 192. https://doi.org/10.3847/1538-4357/ab40a3

Andrews-Hanna, J. C., Asmar, S. W., Head III, J. W., Kiefer, W. S., Konopliv, A. S., Lemoine, F. G., Matsuyama, I., Mazarico, E., McGovern, P. J., Melosh, H. J. and Neumann, G. A. (2013). Ancient igneous intrusions and early expansion of the Moon revealed by GRAIL gravity gradiometry. *Science*, *339*(6120), 675–678. https://doi.org/10.1126/science.1231753

Arakawa, S., Hyodo, R., and Genda, H. (2019). Early formation of moons around large trans-Neptunian objects via giant impacts. *Nat. Astron.*, *3*(9), 802–807. https://doi.org/10.1038/s41550-019-0797-9

Barr, A. C., and Collins, G. C. (2015). Tectonic activity on Pluto after the Charon-forming impact. *Icarus*, *246*, 146–155. https://doi.org/10.1016/j.icarus.2014.03.042

Beddingfield, C. B., Beyer, R. A., Singer, K. N., McKinnon, W. B., Runyon, K., Grundy, W., Stern, S. A., Bray, V., Dhingra, R., … New Horizons Team. (2019). Landslides on Charon. *Icarus*, *335*, 113383. https://doi.org/10.1016/j.icarus.2019.07.017

Bertrand, T., Forget, F., Umurhan, O. M., Grundy, W. M., Schmitt, B., Protopapa, S., Zangari, A. M., White, O. L., Schenk, P. M., … Olkin, C. B. (2018). The nitrogen cycles on Pluto over seasonal and astronomical timescales. *Icarus*, *309*, 277–296. https://doi.org/10.1016/j.icarus.2018.03.012

Beyer, R. A., Nimmo, F., McKinnon, W. B., Moore, J. M., Binzel, R. P., Conrad J. W., Cheng A., Ennico K., Lauer T. R., … Zangari, A. M. (2017). Charon tectonics. *Icarus*, *287*, 161–174. https://doi.org/10.1016/j.icarus.2016.12.018

Beyer, R. A., Spencer, J. R., McKinnon, W. B., Nimmo, F., Beddingfield, C., Grundy, W. M., Ennico, K., Keane, J. T., Moore, J. M., … The New Horizons Team. (2019). The nature and origin of Charon's smooth plains. *Icarus*, *323*, 16–32. https://doi.org/10.1016/j.icarus.2018.12.036

Bierson, C. J., Nimmo, F., and McKinnon, W. B. (2018). Implications of the observed Pluto–Charon density contrast. *Icarus*, *309*, 207–219. https://doi.org/10.1016/j.icarus.2018.03.007

Boyer, S. E., and Elliott, D. (1982). Thrust systems. *AAPG Bull.*, *66*(9), 1196–1230. https://doi.org/10.1306/03B5A77D-16D1-11D7-8645000102C1865D

Brain, D. A., Bagenal, F., Ma, Y. J., Nilsson, H., and Stenberg Wieser, G. (2016). Atmospheric escape from unmagnetized bodies. *Journal of Geophysical Research*: *Planets*, *121*(12), 2364–2385. https://doi.org/10.1002/2016JE005162

Brodzikowski, K., and Van Loon, A. J. (1987). A systematic classification of glacial and periglacial environments, facies and deposits. *Earth-Sci. Rev.*, *24*(5), 297–381. https://doi.org/10.1016/0012-8252(87)90061-4

Byerlee, J. (1978). Friction of rocks. In J. D. Byerlee, et al. (Eds.), *Rock Friction and Earthquake Prediction* (pp. 615-626). Basel: Birkhäuser. https://doi.org/10.1007/978-3-0348-7182-2_4

Canup, R. M. (2005). A giant impact origin of Pluto–Charon. *Science*, *307*(5709), 546–550. https://doi.org/10.1126/science.1106818

Canup, R. M., Kratter, K. M., and Neveu, M. (2021). On the origin of the Pluto system. In S. A. Stern, et al. (Eds.), *The Pluto System After New Horizons* (pp. 475-506).Tucson: University of Arizona Press. https://doi.org/10.2458/azu_uapress_9780816540945-ch021

Carr, M. H., Crumpler, L. S., Cutts, J. A., Greeley, R., Guest, J. E., and Masursky, H. (1977). Martian impact craters and emplacement of ejecta by surface flow. *J. Geophys. Res.*, *82*(28), 4055–4065. https://doi.org/10.1029/JS082i028p04055

Cheng, A. F., Weaver, H. A., Conard, S. J., Morgan, M. F., Barnouin-Jha, O., Boldt, J. D., Cooper, K. A., Darlington, E. H., Grey, M. P., … Taylor, H. W. (2008). Long-range reconnaissance imager on New Horizons. *Space Sci. Rev.*, *140*(1-4), 189–215. https://doi.org/10.1007/s11214-007-9271-6

Clark, C. D. (1993). Mega-scale glacial lineations and cross-cutting ice-flow landforms. *Earth surface processes and landforms*, *18*(1), 1–29. https://doi.org/10.1002/esp.3290180102

Collins, G. C., McKinnon, W. B., Moore, J. M., Nimmo, F., Pappalardo, R. T., Prockter, L. M., and Schenk, P. M. (2010). Tectonics of the outer planet satellites. In T. R. Watters, et al. (Eds.), *Planetary Tectonics* (pp. 264-350). Cambridge: Cambridge University Press. https://doi.org/10.1017/CBO9780511691645.008

Conrad, J. W., Nimmo, F., Beyer, R. A., Bierson, C. J., and Schenk, P. M. (2021). Heat flux constraints from variance spectra of Pluto and Charon using limb profile topography. *J. Geophys. Res.*: *Planets*, *126*(2), e2020JE006641. https://doi.org/10.1029/2020JE006641

Cook, S. J., and Swift, D. A. (2012). Subglacial basins: their origin and importance in glacial systems and landscapes. *Earth-Sci. Rev.*, *115*(4), 332–372. https://doi.org/10.1016/j.earscirev.2012.09.009

Cooke, M. L., and Underwood, C. A. (2001). Fracture termination and step-over at bedding interfaces due to frictional slip and interface opening. *J. Struct. Geol.*, *23*(2-3), 223–238. https://doi.org/10.1016/S0191-8141(00)00092-4

Cruikshank, D. P., Umurhan, O. M., Beyer, R. A., Schmitt, B., Keane, J. T., Runyon, K. D., Atri, D., White, O. L., Matsuyama, I., … Ennico, K. (2019). Recent cryovolcanism in Virgil Fossae on Pluto. *Icarus*, *330*, 155–168. https://doi.org/10.1016/j.icarus.2019.04.023

Desch, S. J., and Neveu, M. (2017). Differentiation and cryovolcanism on Charon: a view before and after New Horizons. *Icarus*, *287*, 175–186. https://doi.org/10.1016/j.icarus.2016.11.037

Elliott-Fisk, D. L. (1987). Glacial geomorphology of the White Mountains, California and Nevada: establishment of a glacial chronology. *Phys. Geogr.*, *8*(4), 299–323. https://doi.org/10.1080/02723646.1987.10642330

Evans, D. J. A., Phillips, E. R., Hiemstra, J. F., and Auton, C. A. (2006). Subglacial till: formation, sedimentary characteristics and classification. *Earth-Sci. Rev.*, *78*(1-2), 115–176. https://doi.org/10.1016/j.earscirev.2006.04.001

Farinella, P., and Davis, D. R. (1996). Short-period comets: primordial bodies or collisional fragments?. *Science*, *273*(5277), 938–941. https://doi.org/10.1126/science.273.5277.938

Fergason, R. L., Hare, T. M., and Laura, J. (2018). HRSC and MOLA blended digital elevation model at 200m v2. Astrogeology PDS Annex, U.S. Geological Survey. https://astrogeology.usgs.gov/search/map/Mars/Topography/HRSC_MOLA_Blend/Mars_HRSC_MOLA_BlendDEM_Global_200mp

Fletcher, R. C., and Hallet, B. (1983). Unstable extension of the lithosphere: a mechanical model for basin-and-range structure. *J. Geophys. Res.: Solid Earth*, *88*(B9), 7457–7466. https://doi.org/10.1029/JB088iB09p07457

Fraser, W. C., Brown, M. E., Morbidelli, A., Parker, A., and Batygin, K. (2014). The absolute magnitude distribution of Kuiper belt objects. *Astrophys. J.*, *782*(2), 100. https://doi.org/10.1088/0004-637X/782/2/100

Fray, N., and Schmitt, B. (2009). Sublimation of ices of astrophysical interest: a bibliographic review. *Planet Space Sci.*, *57*(14-15), 2053–2080. https://doi.org/10.1016/j.pss.2009.09.011

Fretwell, P., Pritchard, H. D., Vaughan, D. G., Bamber, J. L., Barrand, N. E., Bell, R., Bianchi, C., Bingham, R. G., Blankenship, D. D., … Zirizzotti, A. (2013). Bedmap2: improved ice bed, surface and thickness datasets for Antarctica. *Cryosphere*, *7*(1), 375–393. https://doi.org/10.5194/tc-7-375-2013

Funder, S., Kjeldsen, K. K., Kjær, K. H., and Cofaigh, C. Ó. (2011). The Greenland Ice Sheet during the past 300,000 years: a review. *Dev. Quat. Sci.*, *15*, 699–713. https://doi.org/10.1016/B978-0-444-53447-7.00050-7

Gladstone, G. R., Stern, S. A., Ennico, K., Olkin, C. B., Weaver, H. A., Young, L. A., Summers, M. E., Strobel, D. F., Hinson, D. P., … The New Horizons Science Team. (2016). The atmosphere of Pluto as observed by New Horizons. *Science*, *351*(6279), eaad8866. https://doi.org/10.1126/science.aad8866

Goetze, C. (1978). The mechanisms of creep in olivine. *Philos. Trans. Roy. Soc. A: Math., Phys. Sci.*, *288*(1350), 99-119. https://doi.org/10.1098/rsta.1978.0008

Gordon, J. E., Whalley, W. B., Gellatly, A. F., and Vere, D. M. (1992). The formation of glacial flutes: assessment of models with evidence from Lyngsdalen, North Norway. *Quaternary Science Reviews*, *11*(7-8), 709–731. https://doi.org/10.1016/0277-3791(92)90079-N

Grau Galofre, A., Jellinek, A. M., and Osinski, G. R. (2020). Valley formation on early Mars by subglacial and fluvial erosion. *Nat. Geosci.*, *13*(10), 663–668. https://doi.org/10.1038/s41561-020-0618-x

Hansen, C. J., and Paige, D. A. (1996). Seasonal nitrogen cycles on Pluto. *Icarus*, *120*(2), 247–265. https://doi.org/10.1006/icar.1996.0049

Hayes, A. G., Lorenz, R. D., and Lunine, J. I. (2018). A post-Cassini view of Titan's methane-based hydrologic cycle. *Nat. Geosci.*, *11*(5), 306–313. https://doi.org/10.1038/s41561-018-0103-y

Head, J. W., and Wilson, L. (2017). Generation, ascent and eruption of magma on the Moon: New insights into source depths, magma supply, intrusions and effusive/explosive eruptions (Part 2: Predicted emplacement processes and observations). *Icarus*, 283, 176–223. https://doi.org/10.1016/j.icarus.2016.05.031

Helfenstein, P., and Porco, C. C. (2015). Enceladus' geysers: relation to geological features. *Astron. J.*, *150*(3), 96. https://doi.org/10.1088/0004-6256/150/3/96

Holt, J. W., Safaeinili, A., Plaut, J. J., Head, J. W., Phillips, R. J., Seu, R., Kempf, S. D., Choudhary, P., Young, D. A., … Gim, Y. (2008). Radar sounding evidence for buried glaciers in the southern mid-latitudes of Mars. *Science*, *322*(5905), 1235–1238. https://doi.org/10.1126/science.1164246

Howard, A. D., Moore, J. M., Umurhan, O. M., White, O. L., Anderson, R. S., McKinnon, W. B., Spencer, J. R., Schenk, P. M., Beyer, R. A., … The New Horizons Science Team. (2017). Present and past glaciation on Pluto. *Icarus*, *287*, 287–300. https://doi.org/10.1016/j.icarus.2016.07.006

Howett, C. J. A., Parker, A. H., Olkin, C. B., Reuter, D. C., Ennico, K., Grundy, W. M., Graps, A. L., Harrison, K. P., Throop, H. B., … Verbiscer, A. J. (2017). Inflight radiometric calibration of New Horizons' multispectral visible imaging camera (MVIC). *Icarus*, *287*, 140–151. https://doi.org/10.1016/j.icarus.2016.12.007

Hunten, D. M. (1982). Thermal and nonthermal escape mechanisms for terrestrial bodies. *Planetary and Space Science*, *30*(8), 773–783. https://doi.org/10.1016/0032-0633(82)90110-6

Jakobsson, M., Nilsson, J., Anderson, L., Backman, J., Björk, G., Cronin, T. M., Kirchner, N., Koshurnikov, A., Mayer, L., … Semiletov, I. (2016). Evidence for an ice shelf covering the central Arctic Ocean during the penultimate glaciation. *Nat. Commun.*, *7*(1), 10365. https://doi.org/10.1038/ncomms10365

Johnson, P. E., Young, L. A., Protopapa, S., Schmitt, B., Gabasova, L. R., Lewis, B. L., Stansberry, J. A., Mandt, K. E., and White, O. L. (2021). Modeling Pluto's minimum pressure: implications for haze production. *Icarus*, *356*, 114070. https://doi.org/10.1016/j.icarus.2020.114070

Kenyon, S. J., and Bromley, B. C. (2020). Craters on Charon: impactors from a collisional cascade among Trans-Neptunian Objects. *Planet. Sci. J.*, *1*(2), 40. https://doi.org/10.3847/PSJ/aba8a9

King, E. C., Hindmarsh, R. C. A., and Stokes, C. R. (2009). Formation of mega-scale glacial lineations observed beneath a West Antarctic ice stream. *Nat. Geosci.*, *2*(8), 585–588. https://doi.org/10.1038/ngeo581

Kronberg, P., Hauber, E., Grott, M., Werner, S. C., Schäfer, T., Gwinner, K., Giese, B., Masson, P., and Neukum, G. (2007). Acheron Fossae, Mars: tectonic rifting, volcanism, and implications for lithospheric thickness. *J. Geophys. Res.: Planets*, *112*(E4), E04005. https://doi.org/10.1029/2006JE002780

Lavvas, P., Lellouch, E., Strobel, D. F., Gurwell, M. A., Cheng, A. F., Young, L. A., and Gladstone, G. R. (2021). A major ice component in Pluto's haze. *Nat. Astron.*, *5*(3), 289–297. https://doi.org/10.1038/s41550-020-01270-3

Lopes, R. M. C., Mitchell, K. L., Stofan, E. R., Lunine, J. I., Lorenz, R., Paganelli, F., Kirk, R. L., Wood, C. A., Wall, S. D., … Zebker, H. A. (2007). Cryovolcanic features on Titan's surface as revealed by the Cassini Titan Radar Mapper. *Icarus*, *186*(2), 395–412. https://doi.org/10.1016/j.icarus.2006.09.006

Lorenz, R. D., Lopes, R. M., Paganelli, F., Lunine, J. I., Kirk, R. L., Mitchell, K. L., Soderblom, L. A., Stofan, E. R., Ori, G., … The Cassini RADAR Team. (2008). Fluvial channels on Titan: initial Cassini RADAR observations. *Planet. Space Sci.*, *56*(8), 1132–1144. https://doi.org/10.1016/j.pss.2008.02.009

Lucchitta, B. K. (1979). Landslides in Valles Marineris, Mars. *J. Geophys. Res.: Solid Earth*, *84*(B14), 8097–8113. https://doi.org/10.1029/JB084iB14p08097

Malamud, U., Perets, H. B., and Schubert, G. (2017). The contraction/expansion history of Charon with implications for its planetary-scale tectonic belt. *Mon. Not. Roy. Astron. Soc.*, *468*(1), 1056–1069. https://doi.org/10.1093/mnras/stx546

Martin, C. R., and Binzel, R. P. (2021). Ammonia-water freezing as a mechanism for recent cryovolcanism on Pluto. *Icarus*, *356*, 113763. https://doi.org/10.1016/j.icarus.2020.113763

Matsuyama, I., and Nimmo, F. (2013). Pluto's tectonic pattern predictions. In *Proceedings of the 44th Lunar and Planetary Science Conference* (pp. 1399). Texas: LPI Contribution.

McKinnon, W. B. (1989). On the origin of the Pluto–Charon binary. *Astrophys. J. Lett.*, *344*, L41. https://doi.org/10.1086/185526

McKinnon, W. B., Glein, C. R., Bertrand, T., and Rhoden, A. R. (2021). Formation, composition, and history of the Pluto system: a post-*New-Horizons* synthesis. In *The Pluto System After New Horizons* (pp. 507–543). Tucson: University of Arizona Press. https://doi.org/10.2458/azu_uapress_9780816540945-ch022

Mège, D., and Masson, P. (1996). Amounts of crustal stretching in Valles Marineris, Mars. *Planet. Space Sci.*, *44*(8), 749–781. https://doi.org/10.1016/0032-0633(96)00013-X

Moore, J. M., McKinnon, W. B., Spencer, J. R., Howard, A. D., Schenk, P. M., Beyer, R. A., Nimmo, F., Singer, K. N., Umurhan, O. M., … New Horizons Science Team. (2016). The geology of Pluto and Charon through the eyes of New Horizons. *Science*, *351*(6279), 1284–1293. https://doi.org/10.1126/science.aad7055

Morbidelli, A., Nesvorny, D., Bottke, W. F., and Marchi, S. (2021). A re-assessment

of the Kuiper belt size distribution for sub-kilometer objects, revealing collisional equilibrium at small sizes. *Icarus*, *356*, 114256. https://doi.org/10.1016/j.icarus.2020.114256

Morse, Z. R., Osinski, G. R., and Tornabene, L. L. (2018). New morphological mapping and interpretation of ejecta deposits from Orientale Basin on the Moon. *Icarus*, *299*, 253–271. https://doi.org/10.1016/j.icarus.2017.08.010

Nahm, A. L., and Schultz, R. A. (2010). Evaluation of the orogenic belt hypothesis for the formation of the Thaumasia Highlands, Mars. *J. Geophys. Res.: Planets*, *115*(E4), E04008. 10.1029/2009JE003327

Nesvorný, D. (2018). Dynamical evolution of the early Solar System. *Annu. Rev. Astron. Astrophys.*, *56*, 137–174. https://doi.org/10.1146/annurev-astro-081817-052028

Phillips, R. J., Zuber, M. T., Smrekar, S. E., Mellon, M. T., Head, J. W., Tanaka, K. L., Putzig, N. E., Milkovich, S. M., Campbell, B. A., … Marinangeli, L. (2008). Mars north polar deposits: stratigraphy, age, and geodynamical response. *Science*, *320*(5880), 1182–1185. https://doi.org/10.1126/science.1157546

Protopapa, S., Cook, J. C., Grundy, W. M., Cruikshank, D. P., Dalle Ore, C. M., and Beyer, R. A. (2021). Surface composition of Charon. In S. A. Stern, et al. (Eds), *The Pluto System After New Horizons* (pp. 433-456). Tucson: University of Arizona Press. https://doi.org/10.2458/azu_uapress_9780816540945-ch019

Reuter, D. C., Stern, S. A., Scherrer, J., Jennings, D. E., Baer, J. W., Hanley, J., Hardaway, L., Lunsford, A., McMuldroch, S., … Young, L. A. (2008). Ralph: A visible/infrared imager for the New Horizons Pluto/Kuiper Belt Mission. *Space Sci. Rev.*, *140*(1-4), 129–154. https://doi.org/10.1007/s11214-008-9375-7

Rhoden, A. R., Skjetne, H. L., Henning, W. G., Hurford, T. A., Walsh, K. J., Stern, S. A., Olkin, C. B., Spencer, J. R., Weaver, H. A., … The New Horizons Team. (2020). Charon: a brief history of tides. *J. Geophys. Res.: Planets*, *125*(7), e2020JE006449. https://doi.org/10.1029/2020JE006449

Robbins, S. J., Singer, K. N., Bray, V. J., Schenk, P., Lauer, T. R., Weaver, H. A., Runyon, K., McKinnon, W. B., Beyer, R. A., … The New Horizons LORRI, MVIC Instrument Teams. (2017). Craters of the Pluto–Charon system. *Icarus*, *287*, 187–206. https://doi.org/10.1016/j.icarus.2016.09.027

Robbins, S. J., Runyon, K., Singer, K. N., Bray, V. J., Beyer, R. A., Schenk, P., McKinnon, W. B., Grundy, W. M., Nimmo, F., ... Stern, S. A. (2018). Investigation of Charon's craters with abrupt terminus ejecta, comparisons with other icy bodies, and formation implications. *J. Geophys. Res.: Planets*, *123*(1), 20–36. https://doi.org/10.1002/2017JE005287

Robbins, S. J., Beyer, R. A., Spencer, J. R., Grundy, W. M., White, O. L., Singer, K. N., Moore, J. M., Dalle Ore, C. M., McKinnon, W. B., … Stern, S. A. (2019). Geologic landforms and chronostratigraphic history of Charon as revealed by a hemispheric geologic map. *J. Geophys. Res.: Planets*, *124*(1), 155–174. https://doi.org/10.1029/2018JE005684

Robbins, S. J., and Singer, K. N. (2021). Pluto and Charon impact crater populations: reconciling different results. *Planet. Sci. J.*, *2*(5), 192. https://doi.org/10.3847/PSJ/ac0e94

Schenk, P. M., Beyer, R. A., McKinnon, W. B., Moore, J. M., Spencer, J. R., White, O. L., Singer, K., Umurhan, O. M., Nimmo, F., … The New Horizons Geology and Geophysics Investigation Team. (2018a). Breaking up is hard to do: Global cartography and topography of Pluto's mid-sized icy Moon Charon from New Horizons. *Icarus*, *315*, 124–145. https://doi.org/10.1016/j.icarus.2018.06.010

Schenk, P. M., Beyer, R. A., McKinnon, W. B., Moore, J. M., Spencer, J. R., White, O. L., Singer, K., Nimmo, F., Thomason, C., … The New Horizons Geology and Geophysics Investigation Team. (2018b). Basins, fractures and volcanoes: global cartography and topography of Pluto from New Horizons. *Icarus*, *314*, 400–433. https://doi.org/10.1016/j.icarus.2018.06.008

Schlichting, H. E., and Sari, R. (2011). Runaway growth during planet formation: Explaining the size distribution of large Kuiper belt objects. *Astrophys. J.*, *728*(1), 68. https://doi.org/10.1088/0004-637X/728/1/68

Schlichting, H. E., Ofek, E. O., Sari, R., Nelan, E. P., Gal-Yam, A., Wenz, M., Muirhead, P., Javanfar, N., and Livio, M. (2012). Measuring the abundance of sub-kilometer-sized Kuiper belt objects using stellar occultations. *Astrophys. J.*, *761*(2), 150. https://doi.org/10.1088/0004-637X/761/2/150

Schlichting, H. E., Fuentes, C. I., and Trilling, D. E. (2013). Initial planetesimal sizes and the size distribution of small Kuiper belt objects. *Astron. J.*, *146*(2), 36. https://doi.org/10.1088/0004-6256/146/2/36

Schulson, E. M. (2001). Brittle failure of ice. *Eng. Fract. Mech.*, *68*(17-18), 1839–1887. https://doi.org/10.1016/S0013-7944(01)00037-6

Sharp, R. P. (1958). Malaspina glacier, Alaska. *GSA Bull.*, *69*(6), 617–646. https://doi.org/10.1130/0016-7606(1958)69[617:MGA]2.0.CO;2

Singer, K. N., McKinnon, W. B., Gladman, B., Greenstreet, S., Bierhaus, E. B., Stern, S. A., Parker, A. H., Robbins, S. J., Schenk, P. M., … New Horizons Ralph and LORRI Teams. (2019). Impact craters on Pluto and Charon indicate a deficit of small Kuiper belt objects. *Science*, *363*(6430), 955–959. https://doi.org/10.1126/science.aap8628

Singer, K. N., White, O. L., Schmitt, B., Rader, E. L., Protopapa, S., Grundy,W. M., Cruikshank, D. P., Bertrand, T., Schenk, P. M., … Ennico-Smith, K. (2022). Large-scale cryovolcanic resurfacing on Pluto. *Nat. Commun.*, *13*(1), 1542. https://doi.org/10.1038/S41467-022-29056-3

Spencer, J. R., Barr, A. C., Esposito, L. W., Helfenstein, P., Ingersoll, A. P., Jaumann, R., McKay, C. P., Nimmo, F., and Waite, J. H. (2009). Enceladus: an active cryovolcanic satellite. In M. K. Dougherty, et al. (Eds), *Saturn from Cassini-Huygens* (pp. 683-724). Dordrecht: Springer. https://doi.org/10.1007/978-1-4020-9217-6_21

Spencer, J. R., Stern, S. A., Moore, J. M., Weaver, H. A., Singer, K. N., Olkin, C. B., Verbiscer, A. J., McKinnon, W. B., Parker, J. W., … Wasserman, L. H. (2020). The geology and geophysics of Kuiper Belt object (486958) Arrokoth. *Science*, *367*(6481), eaay3999. https://doi.org/10.1126/science.aay3999

Spencer, J. R., Beyer, R. A., Robbins, S. J., Singer, K. N., and Nimmo, F. (2021). The geology and geophysics of Charon. In S. A. Stern, et al. (Eds), *The Pluto System After New Horizons* (pp. 395-412). Tucson: University of Arizona Press. https://doi.org/10.2458/azu_uapress_9780816540945-ch017

Stern, S. A. (1995). Collisional time scales in the Kuiper disk and their implications. *The Astron. J.*, *110*, 856. https://doi.org/10.1086/117568

Stern, S. A., and Trafton, L. M. (2008). On the atmospheres of objects in the Kuiper belt. In *The Solar System beyond Neptune* (pp. 365-380). Tucson: University of Arizona Press.

Stern, S. A., Gladstone, R., Zangari, A., Fleming, T., and Goldstein, D. (2015). Transient atmospheres on Charon and water-ice covered KBOs resulting from comet impacts. *Icarus*, *246*, 298–302. https://doi.org/10.1016/j.icarus.2014.03.008

Stofan, E. R., Elachi, C., Lunine, J. I., Lorenz, R. D., Stiles, B., Mitchell, K. L., Ostro, S., Soderblom, L., Wood, C., … West, R. (2007). The lakes of Titan. *Nature*, *445*(7123), 61–64. https://doi.org/10.1038/nature05438

Trafton, L., Stern, S. A., and Gladstone, G. R. (1988). The Pluto–Charon system: the escape of Charon's primordial atmosphere. *Icarus*, *74*(1), 108–120. https://doi.org/10.1016/0019-1035(88)90033-4

Waller, R. I. (2001). The influence of basal processes on the dynamic behaviour of cold-based glaciers. *Quat. Int.*, *86*(1), 117–128. https://doi.org/10.1016/S1040-6182(01)00054-4

Watkins, J. A., Ehlmann, B. L., and Yin, A. (2015). Long-runout landslides and the long-lasting effects of early water activity on Mars. *Geology*, *43*(2), 107–110. https://doi.org/10.1130/G36215.1

Watkins, J. A., Ehlmann, B. L., and Yin, A. (2020). Spatiotemporal evolution, mineralogical composition, and transport mechanisms of long-runout landslides in Valles Marineris, Mars. *Icarus*, *350*, 113836. https://doi.org/10.1016/j.icarus.2020.113836

Watters, T. R., Selvans, M. M., Banks, M. E., Hauck, S. A., Becker, K. J., Robinson, M. S. (2015). Distribution of large-scale contractional tectonic landforms on Mercury: implications for the origin of global stresses. *Geophys. Res. Lett.*, *42*(10), 3755–3763. https://doi.org/10.1002/2015GL063570

Weertman, J. (1983). Creep deformation of ice. *Annu. Rev. Earth Planet. Sci.*, *11*, 215–240. https://doi.org/10.1146/annurev.ea.11.050183.001243

Weiss, D. K., and Head, J. W. (2013). Formation of double-layered ejecta craters on Mars: a glacial substrate model. *Geophys. Res. Lett.*, *40*(15), 3819–3824. https://doi.org/10.1002/grl.50778

Yamashita, Y., Kato, M., and Arakawa, M. (2010). Experimental study on the rheological properties of polycrystalline solid nitrogen and methane: Implications for tectonic processes on Triton. *Icarus*, *207*(2), 972–977. https:/

/doi.org/10.1016/j.icarus.2009.11.032

Yin, A. (2000). Mode of Cenozoic east-west extension in Tibet suggesting a common origin of rifts in Asia during the Indo-Asian collision. *J. Geophys. Res.*: *Solid Earth*, *105*(B9), 21745–21759. https://doi.org/10.1029/2000JB900168

Yin, A. (2012a). Structural analysis of the Valles Marineris fault zone: possible evidence for large-scale strike-slip faulting on Mars. *Lithosphere*, *4*(4), 286–330. https://doi.org/10.1130/L192.1

Yin, A. (2012b). An episodic slab-rollback model for the origin of the Tharsis rise on Mars: Implications for initiation of local plate subduction and final unification of a kinematically linked global plate-tectonic network on Earth. *Lithosphere*, *4*(6), 553–593. https://doi.org/10.1130/L195.1

Yin, A., and Pappalardo, R. T. (2015). Gravitational spreading, bookshelf faulting, and tectonic evolution of the South Polar Terrain of Saturn's moon Enceladus. *Icarus*, *260*, 409–439. https://doi.org/10.1016/j.icarus.2015.07.017

Yin, A., Moon, S., and Day, M. (2021). Landform evolution of Oudemans crater and its bounding plateau plains on Mars: geomorphological constraints on the Tharsis ice-cap hypothesis. *Icarus*, *360*, 114332. https://doi.org/10.1016/j.icarus.2021.114332

Youdin, A. N., and Goodman, J. (2005). Streaming instabilities in protoplanetary disks. *Astrophys. J.*, *620*(1), 459–469. https://doi.org/10.1086/426895

Zhang, X., Strobel, D. F., and Imanaka, H. (2017). Haze heats Pluto's atmosphere yet explains its cold temperature. *Nature*, *551*(7680), 352–355. https://doi.org/10.1038/nature24465